(12) INTERNATIONAL APPLICATION PUBLISHED UNDER THE PATENT COOPERATION TREATY (PCT)

(19) World Intellectual Property Organization
International Bureau

(43) International Publication Date
02 January 2025 (02.01.2025)

WIPO | PCT

(10) International Publication Number
WO 2025/002236 A1

(51) International Patent Classification:
G01V 1/28 (2006.01) *G01V 1/30* (2006.01)

(21) International Application Number:
PCT/CN2024/101927

(22) International Filing Date:
27 June 2024 (27.06.2024)

(25) Filing Language: English

(26) Publication Language: English

(30) Priority Data:
63/510,624 27 June 2023 (27.06.2023) US

(71) Applicant: **THE UNIVERSITY OF HONG KONG** [CN/CN]; Pokfulam Road, Hong Kong (CN).

(72) Inventor: **LIU, Xin**; Room B4, 8/Floor, Block B Of Belcher Court, 2 Sai Cheung Street, Hong Kong (CN).

(74) Agent: **LIU , SHEN & ASSOCIATES**; 10th Floor, Building 1, 10 Caihefang Road, Haidian District, Beijing 100080 (CN).

(81) Designated States *(unless otherwise indicated, for every kind of national protection available)*: AE, AG, AL, AM, AO, AT, AU, AZ, BA, BB, BG, BH, BN, BR, BW, BY, BZ, CA, CH, CL, CN, CO, CR, CU, CV, CZ, DE, DJ, DK, DM, DO, DZ, EC, EE, EG, ES, FI, GB, GD, GE, GH, GM, GT, HN, HR, HU, ID, IL, IN, IQ, IR, IS, IT, JM, JO, JP, KE, KG, KH, KN, KP, KR, KW, KZ, LA, LC, LK, LR, LS, LU, LY, MA, MD, MG, MK, MN, MU, MW, MX, MY, MZ, NA, NG, NI, NO, NZ, OM, PA, PE, PG, PH, PL, PT, QA, RO, RS, RU, RW, SA, SC, SD, SE, SG, SK, SL, ST, SV, SY, TH, TJ, TM, TN, TR, TT, TZ, UA, UG, US, UZ, VC, VN, WS, ZA, ZM, ZW.

(84) Designated States *(unless otherwise indicated, for every kind of regional protection available)*: ARIPO (BW, CV, GH, GM, KE, LR, LS, MW, MZ, NA, RW, SC, SD, SL, ST, SZ, TZ, UG, ZM, ZW), Eurasian (AM, AZ, BY, KG, KZ, RU, TJ, TM), European (AL, AT, BE, BG, CH, CY, CZ, DE, DK, EE, ES, FI, FR, GB, GR, HR, HU, IE, IS, IT, LT, LU, LV, MC, ME, MK, MT, NL, NO, PL, PT, RO, RS, SE, SI, SK, SM, TR), OAPI (BF, BJ, CF, CG, CI, CM, GA, GN, GQ, GW, KM, ML, MR, NE, SN, TD, TG).

Published:
— *with international search report (Art. 21(3))*

(54) Title: AMBIENT NOISE DIFFERENTIAL ADJOINT TOMOGRAPHY SYSTEM

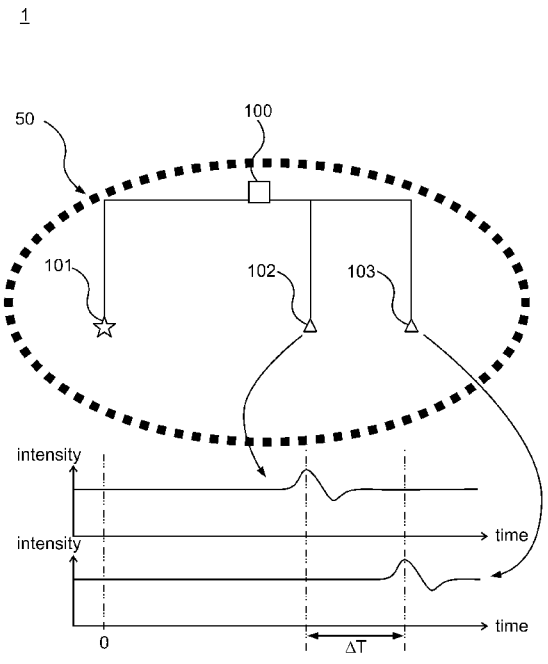

FIG. 1

(57) Abstract: An ambient noise differential adjoint tomography system(l) is provided. The system(l) comprises seismic wave recording devices(101,102,103) and a processor) 100). The processor) 100) indicates three of the seismic wave recording devices(101,102,103) as a source(lOl), a first receiver) 102), and a second receiver) 103), and the source(lOl) and the first and second receivers (102, 103) are arranged as a linear array, and the first and second receivers(102,103) are positioned nearby each other. The processor) 100) receives seismic noise and obtain a noise interferometry, computing synthetic dispersive surface wave signals, generating a differential adjoint tomography based on observed dispersive surface wave from the noise interferometry. The processor) 100) estimates a shear wave velocity from the differential adjoint tomography, using the estimated tomography to estimate the characteristic of the region, and the processor) 100) provide a diagram with characteristic of the region through a display or printer.

WO 2025/002236 A1

AMBIENT NOISE DIFFERENTIAL ADJOINT TOMOGRAPHY SYSTEM

Field of the Invention:

[0001] The present invention generally relates to a tomography system. More specifically the present invention relates to an ambient noise differential adjoint tomography system.

Background of the Invention:

[0002] Water and oil resources are essential for human beings and the current exploration of these resources is primarily based on active-source seismic surveys. Active-source seismic surveys are used both on land and in the ocean to explore what lies beneath the Earth's surface. On land, shockwaves (created by small explosions or heavy hammer impacts) travel through the ground, bouncing back when they encounter different materials. Sensors detect these returning waves, helping geophysicists create subsurface images for resource exploration. In the ocean, large air guns generate underwater shockwaves, which penetrate the ocean floor. Instruments on the ocean floor record these waves, allowing researchers to map layers beneath the seabed and locate oil and gas reserves.

[0003] Water and oil resources are essential for human survival, and their exploration relies heavily on active-source seismic surveys. These surveys are conducted both on land and in the ocean to investigate what lies beneath the Earth's surface.

[0004] **On Land**

[0005] Active-source seismic surveys on land involve generating shockwaves using small explosions or heavy hammer impacts. These shockwaves travel through the ground and reflect back when they encounter different subsurface materials. Sensors placed on the surface detect these returning waves. The data collected helps geophysicists create detailed images of the subsurface, which are crucial for resource exploration.

[0006] **In the Ocean**

[0007] In marine environments, large air guns are used to generate underwater shockwaves. These shockwaves penetrate the ocean floor, and instruments on the ocean floor record the returning waves. This information allows researchers to map the layers beneath the seabed, helping locate oil and gas reserves.

[0008] By using these active-source seismic survey techniques, geophysicists can effectively explore and map the Earth's subsurface, identifying valuable water and oil resources.

[0009] Active-source seismic surveys have several limitations in resource exploration:

[0010] Firstly, they can have a potential environmental impact on marine life. The use of large air guns underwater can disturb or harm marine animals, which raises ecological concerns.

Secondly, these surveys are expensive due to the need for specialized equipment and extensive logistical support. This high cost can limit the number and scope of surveys that can be conducted.

[0011] Additionally, active-source surveys often have a limited coverage area. The logistics and costs involved mean that only specific regions can be surveyed, potentially leaving gaps in the exploration data. In urban areas, the use of explosive sources or heavy equipment can cause disturbances, leading to opposition from local communities and restrictions on where and when surveys can be conducted.

[0012] Finally, conducting active-source seismic surveys involves strict regulatory compliance. These surveys are subject to rigorous regulations to ensure safety and environmental protection, which can add to the complexity and cost of conducting them.

[0013] Overall, while active-source seismic surveys are a powerful tool for resource exploration, these limitations highlight the need for alternative or complementary methods to overcome these challenges.

[0014] In general, active-source seismic surveys primarily focus on the P-wave velocity of the underground structure. This is because the P-waves, or primary waves, are easier to generate and record using conventional seismic sources like airguns in the ocean and explosives or hammers on land.

[0015] However, performing S-wave tomography using active-source surveys for subsurface structures under the seafloor is not possible because the airgun shots at the ocean surface do not generate S-waves. S-waves, or shear waves, require different mechanisms to be generated and do not propagate well through liquids, making it difficult to study them in marine environments using traditional methods.

[0016] On land, S-wave tomography is also challenging due to interference from scattered waves near the S-wave phases generated by active sources. This scattering can complicate the interpretation of the data and reduce the accuracy of the resulting subsurface models.

[0017] Despite these challenges, S-wave tomography is more sensitive to fluid reservoirs than P-wave tomography. S-waves are more affected by the presence of fluids in the subsurface, making them crucial for accurate detection and characterization of water and oil reservoirs. Therefore, it is essential to perform S-wave tomography for comprehensive exploration and assessment of these valuable resources.

[0018] Recently, researchers have been working to advance seismic imaging techniques and address the limitations of traditional methods using ambient noise tomography.

[0019] Ambient noise tomography is a powerful technique used to explore the shallow Earth structure and can potentially be a cost-effective way of exploring water and oil resources. This method leverages continuous, globally distributed sources of ambient seismic noise, such as ocean waves, wind, and other environmental factors.

[0020] Traditional ambient noise tomography methods employ ray theory to invert 2D group or phase velocity maps and reconstruct 3D tomography models for S-waves.

[0021] Ray theory is analogous to shooting a laser beam through a fish tank, where the light beam bends at the air-water interface. This bending is similar to how seismic waves refract at boundaries between different subsurface layers. Ray theory provides a high-frequency approximation of seismic wave propagation in the Earth's medium, effectively capturing how seismic waves travel through various geological structures.

[0022] By using this approach, ambient noise tomography can create detailed images of the subsurface, revealing important information about the S-wave velocity structure.

[0023] Previous studies of S-wave velocity structure have primarily relied on ray-theoretical approaches. In these methods, a phase velocity profile along the seismic array is first created. This profile is then interpreted using a 1D S-wave velocity tomography with depth, assuming a layered-cake model at each horizontal geographic location. This approach simplifies the subsurface into discrete layers, each with uniform properties, to estimate the S-wave velocity at various depths.

[0024] The noise sources are unevenly distributed in space and time. As a result, variations in the distribution of noise sources can cause time shifts in the signals derived from ambient noise cross-correlations. This inconsistency makes traditional ambient noise tomography unable to accurately delineate the extent of water or oil in reservoir rocks. Consequently, the uneven noise distribution leads to inaccuracies in identifying and mapping subsurface fluid reservoirs.

[0025] Due to the limitations of ray theory and the spatially uneven distribution of noise sources, traditional ambient noise tomography cannot effectively reveal fluid-rich structures underground. As a result, a more advanced technique is needed to accurately detect water and oil resources using ambient noise data.

Summary of the Invention:

[0026] In some embodiments of the present invention, ambient noise differential adjoint tomography system has been developed to infer the near-surface S-wave velocity structure beneath seismic stations. This advanced technique enhances the accuracy and detail of

subsurface imaging by utilizing ambient noise data and addressing the limitations of traditional methods.

[0027] In some embodiments of the present invention, the ambient noise differential adjoint tomography system utilizes frequency-dependent differential time measurements between pairs of nearby stations for a relatively more distant virtual earthquake source, which is randomly selected from one of the stations. This approach enhances the accuracy of subsurface imaging by considering the variations in seismic wave travel times across different frequencies and distances.

[0028] The ambient noise differential adjoint tomography system of the present invention has several advantages over traditional ambient noise ray-theoretical or adjoint tomography approaches:

[0029] **Insensitivity to Noise Source Distribution**: It is insensitive to the unknown spatio-temporal distribution of noise sources, which helps in reducing biases caused by unevenly distributed ambient noise sources.

[0030] **Wave Equation and Finite-Frequency Effects**: It incorporates the wave equation and finite-frequency effects, allowing for a more accurate representation of seismic wave propagation that is not limited by the flat-layer assumption used in 1D depth velocity tomography and ray theory.

[0031] **Unbiased S-Wave Velocity Tomography**: It directly performs unbiased S-wave velocity tomography using ambient noise differential-time data and the wave equation, providing more accurate and detailed subsurface imaging.

[0032] In an embodiment of the present invention, an ambient noise differential adjoint tomography system is provided. The system comprises: a plurality of seismic wave recording devices, and a processor. The seismic wave recording devices are disposed on a region. The processor connects the seismic wave recording devices. The processor indicates three of the seismic wave recording devices as a source, a first receiver, and a second receiver, and the source and the first and second receivers are arranged as a linear array, and the first and second receivers are positioned nearby each other. The processor receives seismic noise from the source, the first receiver, and the second receiver and obtain a noise interferometry. The processor compute synthetic dispersive surface wave signals with the source and the first and second receivers. The processor generates a differential adjoint tomography based on observed dispersive surface wave from the noise interferometry. The processor estimates a shear wave velocity from the differential adjoint tomography. The processor uses the estimated

tomography to estimate the characteristic of the region, and the processor provide a diagram with characteristic of the region through a display or printer.

[0033] In another embodiment of the present invention, an ambient noise differential adjoint tomography system is provided. The system comprises a plurality of seismic wave recording devices and a processor. The seismic wave recording devices are disposed on a region. The processor connects the seismic wave recording devices. The processor indicates three of the seismic wave recording devices as a source, a first receiver, and a second receiver, and the first and second receivers are disposed nearby while each of them have different distance measuring from the source, and the source is disposed far away from the receivers, and the source and the receivers are linearly disposed. The source and the receivers record ambient noise and generate ambient noise data. The the processor compute a seismic noise interferometry by cross-correlating the ambient noise data from the source and the receivers to generate virtual earthquake signals. The the processor measures the observed differential times between the virtual earthquake signals for receivers at different frequencies. The processor creates an initial S wave velocity model based on existing information or assumptions. The processor simulates synthetic waveforms using the initial velocity model and compute the corresponding synthetic differential times. The processor calculates the misfit between the observed and synthetic differential times. The processor compute the gradient of the misfit function using the adjoint method, which involves simulating the forward and backward propagation of seismic waves. The processor updates the S wave velocity model iteratively by minimizing the misfit between the observed and synthetic differential times. The processor repeates the steps above until the misfit is sufficiently small or a desired level of convergence is achieved. The processor obtains the final S wave velocity model that best explains the observed differential times, and the processor present the S wave velocity model in diagrams with a display or printer.

[0034] In an embodiment of the present invention, a first distance is between the first and second receivers, and a second distance is the minimal distance between the source and one of the first and second receivers. A ratio of the first and second distances ranges from 1% to 30% and the upper bound of the ratio can be slightly increased. For some sparse seismic arrays, ratio of the first and second distances ranges from 1% to 35%.

[0035] In an embodiment of the present invention, a first reference line is a straight line connecting the source and the first receiver, and a second reference line is a straight line connecting the source and the second receiver. An included angle included by the first reference line and the second reference line is less than 5 degrees.

[0036] In an embodiment of the present invention, a third distance is between the source and the first receiver, and a fourth distance is between the source and the second receiver. The fourth distance is less than 1.25 times of the third distance.

[0037] In an embodiment of the present invention, the characteristic comprises actual underground geophysical property or hydrological property of the region.

[0038] In an embodiment of the present invention, the seismic wave recording devices comprise 42 seismographs, and the seismographs are disposed across the Los Angeles Basin.

[0039] In an embodiment of the present invention, the seismic wave recording devices form a linear ocean bottom seismometer (OBS) array, and the OBS array is disposed across the Nankai Trough off the Kii Peninsula, Japan.

[0040] In some embodiments of the present invention, a new cost-effective system is developed, ambient noise differential adjoint tomography , which significantly improves the sensitivity to fluid-bearing rocks by cancelling bias caused by unknown noise sources and helps manage groundwater resources effectively. This system is used to image the shallow shear-wave velocity structure beneath a linear seismic array across the Los Angeles Basin. Shear-wave velocity tomography shows significant velocity reduction marking the location of a major regional water producer – the Silverado aquifer – along with the other deeper fluid-bearing structures. In addition, the porosity, or its lower bound, is derived between a depth range of 0.8-2 km, for a 10-km wide cross-section in Long Beach by calculating the P- and S- wave velocity ratios, which indicates that the sedimentary rock from 1-2 km depth surrounding the Newport-Inglewood Fault contains abundant fluids with pore-fluid fraction ~0.33. The high-porosity rock around the fault coincides with previously observed week-long shallow seismicity aligned with the fault trace 1-5 km south of the LASSIE array in Long Beach.

Brief Description of the Drawings:

[0041] Embodiments of the invention are described in more details hereinafter with reference to the drawings, in which:

[0042] FIG. 1 depicts a conceptual figure of an embodiment of the present invention and its applications. It shows the concepts of ambient noise correlations between one source and two receivers;

[0043] FIG. 2 depicts another conceptual figure of an embodiment of the present invention and its applications. It shows the land application of ambient noise differential adjoint tomography system with differential time measurements;

[0044] FIG. 3 depicts another conceptual figure of an embodiment of the present invention and its applications. It depicts the ocean-bottom application of the ambient noise differential adjoint tomography system;

[0045] FIG. 4 depicts a flow diagram of ambient noise differential adjoint tomography according to an embodiment of the present disclosure;

[0046] FIG. 5 depicts a flow diagram of ambient noise differential adjoint tomography according to another embodiment of the present disclosure;

[0047] FIG. 6 depicts a schematic view of three seismic wave recording devices of an ambient noise differential adjoint tomography system according to an embodiment, and it depicts differential time measurements for a seismic wave recording devices triplet: one source and a pair of receivers;

[0048] FIG. 7 depicts a schematic view of a source, a plurality of noise sources, and a plurality of seismicwave recording devices, depicting geometry for the forward simulation: one virtual source and a subarray;

[0049] FIG. 8 depicts noise source intensity distribution versus azimuth for the synthetic noise interferometry data;

[0050] FIG. 9 depicts inverted velocity based on interferometric differential time kernel;

[0051] FIG. 10 depicts estimated velocity based on point-source differential time kernel;

[0052] FIG. 11A depicts structure kernel for virtual source N101 and receiver pair 21-23; Station N101 is in the SW corner of the LASSIE array; Stations are numbered consecutively from SW corner;

[0053] FIG. 11B depicts structure kernel for virtual source N101 and receiver pair 25-27;

[0054] FIG. 11C depicts combined sensitivity kernel for the virtual source N101 and all station triplets;

[0055] FIG. 12 depicts map of the LASSIE array and regional faults. The red dot is the location of LBCC drilled well. The 5 black triangles are the virtual sources for the validation dataset. The open triangles are the virtual sources for the training dataset. Black lines: faults (dashed if blind);

[0056] FIG. 13 depicts topography along the LASSIE array with fault locations (top) and total sensitivity for all 36 virtual sources in the training set at the initial evaluation of the kernel (bottom);

[0057] FIG. 14 depicts total sensitivity for all 36 virtual sources at the 13th evaluation of the kernel, which uses the optimal velocity model that minimize the validation set;

[0058] FIG. 15 depicts training and validation misfit (loss) functions versus iteration; the optimal velocity parameter is reached at the 13th iteration, where the validation misfit is minimum;

[0059] FIG. 16A depicts topography along the LASSIE array with labels of fault locations (top). NIF:Newport-Inglewood Fault; LAF: Los Alamitos Fault; NF: Norwalk Fault; LEPTF: Lower Elysian Park Thrust Fault. Initial S wave velocity model based on ray theory (bottom);

[0060] FIG. 16B depicts shear wave velocity based on differential adjoint tomography and low frequency data (top). Velocity update for the top panel compared with initial ray theory model (bottom);

[0061] FIG. 16C depicts shear wave velocity based on differential adjoint tomography and low+high frequency data (top). Velocity update for the top panel compared with initial ray theory model (bottom);

[0062] FIG. 17 depicts P and shear wave velocity ratio in Long Beach section (top). Inferred porosity at 0.8 km depth converted from Vp/Vs ratio for pure sand (red dashed line), pure clay (blue dashed line) and half sand-half clay (black solid line), respectively (bottom);

[0063] FIG. 18 depicts topography along the LASSIE array with labels of fault locations. The fault acronyms the same as in FIG. 16A (top). Comparison between inverted shear wave velocity in the top 100 m and geotechnical layer Vs 30 (bottom);

[0064] FIG. 19 depicts the lower bound of porosity converted from Vp/Vs ratio using BGTL method. At 0.8 km depth, the porosity is exact. For depth below 0.8 km, the displayed porosity value is a lower bound;

[0065] FIG. 20 is the Map of a linear ocean-bottom seismic station array off Kumano and shallow slow earthquakes (red & green dots). The southern Kumano Basin is between OBS74 and OBS79;

[0066] FIG. 21 is the S wave tomography result based on this invention. The red color denotes slower S wave velocity, which corresponds to fluid-rich rocks below the sea floor. The tomography is overlaid by seismic reflection profile from active-source data, which shows agreements between our invention method and the active-source method highlighting Kumano sedimentary basin.

Detailed Description:

[0067] In the following description, an ambient noise differential adjoint tomography system and the likes are set forth as preferred examples. It will be apparent to those skilled in the art that modifications, including additions and/or substitutions may be made without

departing from the scope and spirit of the invention. Specific details may be omitted so as not to obscure the invention; however, the disclosure is written to enable one skilled in the art to practice the teachings herein without undue experimentation.

[0068] A major issue in other ambient noise adjoint tomography is that the noise interferometry results depend on both the noise sources and the structural properties they aim to investigate. Given the complex nature of the Earth's heterogeneous ambient seismic field and its temporal variations, the results are inevitably biased by the distribution and characteristics of the noise sources.

[0069] In an embodiment of the present invention, an ambient noise differential adjoint tomography system is provided. The ambient noise differential adjoint tomography system comprises a plurality of seismic wave recording devices and a processor. The processor connects the seismic wave recording devices. While the seismic wave recording devices record the noise in a region, the processor indicates three of the seismic wave recording devices as a source and two receivers.

[0070] The source and the receivers are arranged as a linear array, and the receivers are positioned nearby each other. The processor generates seismic noise at the sources and records at the receivers, and obtaining a noise interferometry, and generating synthetic dispersive surface wave signals, i.e. virtual earthquake signals.

[0071] The relationship between virtual earthquake signals and noise interferometry is based on the concept of Green's function retrieval. In seismic interferometry, cross-correlating the ambient noise recordings between two seismic stations can yield the Green's function, which represents the impulse response of the Earth between these two stations. The resulting cross-correlation function can be interpreted as a virtual earthquake signal, as if one of the stations acts as a virtual source and the other as a receiver. This virtual earthquake signal contains information about the seismic wave propagation between the two stations, including the effects of the Earth's structure along the path. By measuring the time delay (or differential time) between virtual earthquake signals recorded by different pairs of stations, researchers can extract information about the subsurface structure and construct tomographic images, such as those obtained through ambient noise differential adjoint tomography.

[0072] The processor generates a differential adjoint tomography based on observed dispersive surface wave from the noise interferometry. The preocessore estimates a shear wave velocity from the differential adjoint tomography, and the processor use the estimated tomography to estimate the characteristic of the region, providing a diagram with these information through a display or printer.

[0073] FIG. 1 is a schematic view of the ambient noise differential adjoint tomography system according to the embodiment. Referring to FIG. 1, the system 1 uses differential time measurements of a pair of stations within a linear triplet to obtain results that are more sensitive to the structural properties of the medium of the region.

[0074] Referring to FIG. 1, the system 1 comprises seismic wave recording devices including the seismic wave recording devices 101, 102, 103, which form the linear triplet, and these devices 101, 102, 103 and a processor 100 is connected.

[0075] In this embodiment, the system 1 has other seismic wave recording devices, which is not shown in FIG. 1, arranged with these devices 101, 102, 103, and the processor 100 is connected to all the seismic wave recording devices. All of these seismic wave recording devices are recording seismic wave in a land region or marine region, which means the seismic wave recording devices are surrounded by the noise sources 50. The processor 100 indicates these three seismic wave recording device 101, 102, 103 for the following application.

[0076] The processor 100 indicates the device 101 as a source; the device 102 as a receiver; and the device 103 as another receiver. In FIG.1, by cross correlating the ambient noise recordings, which can be generated from any of the noise sources 50, between the source 101 and the stations 102, 103, the processor 100 creates two virtual earthquake signals, as if the source 101 is the earthquake source while the two stations 102, 103, are the receivers of the earthquakes.

[0077] In FIG. 1, diagrams of the two virtual earthquake signals are shown. Notably, there is a time delay (differential time), ΔT, between the virtual earthquake signals recorded by the two stations 102 and 103. This differential time, ΔT, is frequency-dependant and reduces the sensitivity to the unknown spatio-temporal distribution of noise sources. This significantly improves the tomography accuracy and sensitivity to fluid-bearing rocks.

[0078] FIG. 2 is another schematic view of the ambient noise differential adjoint tomography system on the land according to another embodiment. In FIG. 2, the land acquisition geometry is shown. Any station (triangle) can be picked as the virtual source. These stations are connected by a processor as well, which is not shown in this figure, and the processor indicates the source 101, the receiver 102, and the receiver 103. The system cross correlate the ambient noise recordings on the source 101 with that of the receivers 102, 103, generating virtual earthquake signals V1, V2 from the source 101 to the receivers 102, 103. By measuring the differential time ΔT between nearby station pairs, i.e. receivers 102, 103, the system can perform unbiased ambient noise differential adjoint tomography and derived the S

wave tomography image for the subsurface structure underneath the seismic wave recording devices.

[0079] In this description, "S wave" indicates the secondary waves, which is the shear wave mocing particles perpendicular to the direction of wave travel. The seismic wave recorded by the system of the embodiments of the present invention comprises at least the S wave and the P wave, i.e. primary wave.

[0080] In other words, S waves, also known as shear waves or secondary waves, are a type of elastic wave that propagates through the Earth's interior. Unlike P waves (primary waves), which are compressional and can travel through both solids and fluids, S waves are transverse waves that can only travel through solid materials. The particle motion of S waves is perpendicular to the direction of wave propagation. S waves travel slower than P waves and cannot pass through liquid or gas because these materials do not support shear stress. In seismology, the velocity of S waves provides valuable information about the Earth's interior structure, particularly in identifying and characterizing fluid-bearing rocks, as fluids significantly slow down S wave propagation.

[0081] For land applications, in an embodiment of the present invention, the system comprises a linear seismic array consisting of 42 seismographs across the Los Angeles Basin. The tomography results revealed that rocks near the Newport-Inglewood Fault contain substantial fluid, which may facilitate small earthquakes. The study also imaged the Silverado aquifer and identified high-porosity rock associated with shallow seismic activity in Long Beach.

[0082] FIG. 3 is another schematic view of the ambient noise differential adjoint tomography system on the marine region according to another embodiment. In FIG.3, the marine acquisition geometry is shown. The stations, or ocean-bottom seismometers (OBS) or ocean-bottom cables (OBC) are deployed on the sea floor recording seismic noise. Any ocean-bottom seismic station can be picked as the source 101. Then we cross correlate the ambient noise recordings on the source 101 with that of other stations, i.e. receivers 102, 103, generating virtual earthquake signals V1, V2 from the source 101 to the receivers 102, 103. By measuring the differential time ΔT between nearby station pairs 102, 103, we can perform unbiased ambient noise differential adjoint tomography and derived the S wave tomography image for the subsurface structure underneath the ocean-bottom seismic station array below sea floor. This is useful for offshore oil reservoir exploration.

[0083] For marine applications, in another embodiment of the present invention, the system comprises a linear ocean-bottom seismometer (OBS) array across the Nankai Trough off the

Kii Peninsula, Japan. The tomography results indicate that the southern Kumano Basin in the Nankai Trough (SW Japan) has significantly lower S-wave velocities compared to the northern Kumano Basin. This suggests an abundance of fluids in the southern basin, which lies above the weak interplate coupling zone. In contrast, the northern basin overlies the strong interplate coupling zone where slow earthquakes are rarely observed.

[0084] FIG.4 is a flowchart showing the general workflow of ambient noise differential adjoint tomography from seismic noise interferometry (cross correlations) to S wave velocity tomography result according to an embodiment.

[0085] FIG.5 is another flowchart showing detailed workflow of ambient noise differential adjoint tomography according to another embodiment. After seismic data acquisition from a seismic array, i.e. seismic wave recording devices, and seismic noise interferometry computations, the processor of the system of this embodiment measure a observed differential time with dispersion from the noise interferometry.

[0086] The observed differential time data from noise interfereometry is compared with the synthetic differential time data generated by simulated earthquake waveform data using a computer software by numerically solving the elastic seismic wave equation. The loop in FIG. 5 means iterative updates of the S wave velocity model below the seismic array. After the discrepancy between the observed and simulated differential time data is minimized, the tomography result is the final S wave velocity model.

[0087] FIG. 6 is a schematic view of the seismic wave recording devices of a ambient noise differential adjoint tomography system according to an embodiment. Referring to FIG. 6, three stations, i.e. seismic wave recording devices, of this embodiment are linearly disposed. Source 101 is a station indicated as a virtual source in seismic interferometry. Source 101 and receiver 103 has a distance d2 in-between, and source 101 and receiver 102 has a distance d1 in-between. Distance d2 is slightly longer than distance d1.

[0088] To ensure maximum overlap of the Fresnel zones of these two receiver pairs 102, 103, where noise soureces influence the most to measurements, the source 101 and the receivers 102, 103 of this embodiment are chosen such that the distance d2 is less than 125% of the distance d1.

[0089] A straight reference line is shown in FIG. 6 between the source 101 and the receiver 102, and another straight reference line is also shown in FIG. 6 between the source 101 and the receiver 103. An angle A1 included by the reference lines should be less than 5 degrees.

[0090] By taking the differential time measurements for the noise interferometric functions from the pair of source 101 and receiver 103 and the pair of source 101 and receiver 102, the source

kernel sensitivity within the overlapping area is effectively cancelled, and the processor creates a misfit function that is more sensitive to structural properties between receivers 102, 103.

[0091] To be specific, the distance between stations 101 and 103 is slightly longer than the distance between stations 101 and 102, ensuring that the paths from the virtual source to the two receivers have significant overlap.

[0092] By measuring the differential time (i.e., the time difference) between the noise interferometry signals from the station pairs 101-103 and 101-102, the sensitivity to the noise source distribution within the overlapping region is effectively canceled out. This allows the creation of a misfit function that is more sensitive to the structural properties of the Earth between receivers 102 and 103.

[0093] In other words, by focusing on the differential time measurements, rather than the absolute travel times, the method becomes less dependent on the specific distribution of noise sources and more responsive to the seismic velocity structure in the region of interest, particularly between the two receivers 102, 103.

[0094] Differential time sensitivity kernels of noise interferometry functions are effective when the heterogeneous noise source distribution is unknown. Furthermore, the point source kernel is equivalent to the noise interferometry kernel for uniform noise sources, allowing simplifications by replacing the virtual source with a point source while still using differential time measurements. This extends ambient noise differential time kernels to linear arrays lacking 2D seismic wave recording devices coverage.

[0095] In seismology, a sensitivity kernel is a mathematical function that describes how sensitive a seismic measurement (such as travel time or amplitude) is to changes in the Earth's properties (such as seismic wave velocity) at different locations. In other words, it shows how much the measurement would change if there were a small change in the Earth's properties at a specific location.

[0096] When the distribution of noise sources generating ambient seismic noise is not uniform and not well known, using differential time measurements between pairs of stations can help reduce the influence of this unknown noise source distribution on the seismic imaging results. The differential time sensitivity kernels describe how sensitive these differential time measurements are to changes in the Earth's properties.

[0097] The differential time sensitivity kernel for noise interferometry (where virtual earthquake sources are created by cross-correlating ambient noise recorded at different stations) is similar to the sensitivity kernel for a case where there is a single point source generating seismic waves, if the noise source distribution is uniform. This means that even if the actual

noise source distribution is not uniform, we can still use the simpler point source kernel in our calculations, as long as we use differential time measurements.

[0098] This finding is particularly useful when working with linear arrays of seismic stations, where the stations are arranged in a line rather than covering a 2D area. In such cases, using the point source kernel simplifies the computations and allows us to apply the ambient noise differential time analysis to study the Earth's structure along the line of stations, even if we don't have detailed knowledge of the noise source distribution.

[0099] In summary, the sensitivity kernel is a key concept in seismic imaging that helps relate seismic measurements to the Earth's properties. Using differential time sensitivity kernels and replacing virtual sources with point sources can simplify the analysis of ambient seismic noise and extend its applicability to linear seismic arrays, even when the distribution of noise sources is unknown.

[0100] FIG. 7 depicts a schematic view of a source, a plurality of noise sources, and a plurality of stations, i.e. seismic wave recording devices. Referring to FIG. 7, an approximation is demonstrated using synthetic tests. The setup for the forward simulation includes a virtual source and a subarray of 8x8 stations, surrounded by a ring of noise sources. Within the subarray, there is a lamda-shaped low-velocity structure.

[0101] Referring to FIG. 8, the noise source intensity distribution varies with direction, being strongest in the SW direction and zero in the NE direction.

[0102] Based on the simulated data, the velocity anomaly structure is estimated with two approaches:

1. assuming unknown noise source distribution, uniform noise source distribution with interferometric differential time kernels is used to perform adjoint tomography (FIG. 9);
2. replacing the virtual source by a point source, differential time adjoint tomography is performed with point source kernels (FIG. 10).

[0103] The adjoint tomography results for both cases are nearly identical with minor differences in the side lobes, suggesting that the interferometric kernel for uniform noise sources is equivalent to point source kernel for differential time kernels subject to the distance and direction criteria for linear station triplets, i.e. seismic wave recording devices, in the embodiments of the present invention.

[0104] Here, the key formula is briefly reviewed for differential time kernels for a point source. For non-dispersive signal, the misfit function is firstly defined for differential time measurements,

$$\chi_{23}^{dd} = \frac{1}{2}\left[\Delta t_{23} - \Delta t_{23}^{obs}\right]^2, \quad (1)$$

[0105] Misfit function (Eq. 1) is a measure of the difference between the observed data (differential time at different frequency) and the synthetic differential time predicted by a model using wave equations. It is used in optimization problems to find the best model that fits the observed data.

[0106] The variation of the misfit function is expressed as an integral part over the sensitivity kernels,

$$\delta\chi_{23}^{dd} = \int_{\Omega}\left[K_C^{dd}(\mathbf{x})\frac{\delta C}{C} + K_\rho^{dd}(\mathbf{x})\frac{\delta\rho}{\rho}\right]d\mathbf{x}, \quad (2)$$

where K_C^{dd} is the sensitivity kernel for the elastic tensor $C(\mathbf{x})$, K_ρ^{dd} is the sensitivity kernel for density.

[0107] In an ambient noise differential adjoint tomography system, the processor computes the gradient of the misfit function using the adjoint method, which involves simulating the forward and backward propagation of seismic waves. We would like to explain the detail of the approach of the embodiment.

[0108] The following equations (3) and (4) define how to compute inner product between the forward and backward (adjoint) wavefields in order to estimate sensitivity kernel, which is the gradient of data misfit function with respect to the specific elastic modulus (e.g. shear modulus in the examples). The forward wavefield is just created by a point source with a simple source wavelet covering the frequency range of interest from a seismic survey.

[0109] The differential time sensitivity kernel is the interaction between the forward wavefield $\mathbf{u}(\mathbf{x})$ and the adjoint wavefield $\mathbf{u}^\dagger(\mathbf{x})$,

$$K_C^{dd}(\mathbf{x}) = -C(\mathbf{x})\int_f \nabla\mathbf{u}(\mathbf{x},\omega)\left[\nabla\mathbf{u}_3^\dagger(\mathbf{x},\omega) - \nabla\mathbf{u}_2^\dagger(\mathbf{x},\omega)\right]d\omega, \quad (3)$$

where $\mathbf{u}^\dagger$ and $\mathbf{u}^\dagger$ are two adjoint wavefields from locations $\mathbf{x}_3$ and $\mathbf{x}_2$, respectively.

[0110] For SH waves (e.g., Love waves) propagating in a 2D cross-section along a line, the above vector wavefield u(x) reduces to displacement in crossline direction, uy. Suppose the medium is isotropic, the differential sensitivity kernel is considered for shear modulus μ,

$$K_\mu^{dd}(\mathbf{x}) = -\mu(\mathbf{x})\int_f \nabla u_y(\mathbf{x},\omega)\cdot\left[\nabla u_{y3}^\dagger(\mathbf{x},\omega) - \nabla u_{y2}^\dagger(\mathbf{x},\omega)\right]d\omega, \quad (4)$$

where the dot represents vector inner product.

[0111] Referring to FIG. 7, for dispersive seismic waves, the definition of differential time misfit functions for one station triplet is:

$$\chi_{ij}^{dd} = \frac{1}{2}\sum_{\omega} W(\omega)\left[\Delta t_{ij}(\omega) - \Delta t_{ij}^{obs}(\omega)\right]^2, \quad \text{(S1)}$$

where ij

$\Delta t_{ij}^{obs}(\omega)$ and $\Delta t_{ij}(\omega)$ are, respectively, observed and synthetic differential time measurements between station pairs 1-2 and 1-3 ($i \equiv$ station 2 ; $j \equiv$ station 3). Here $W(\omega)$ is a weighting function and ω is angular frequency.

[0112] The variation of misfit function for a station triplet is,

$$\delta\chi_{ij}^{dd} = \sum_{\omega} W(\omega)\left[\Delta t_{ij}(\omega) - \Delta t_{ij}^{obs}(\omega)\right]\delta\Delta t_{ij}(\omega). \quad \text{(S6)}$$

To convert the variation of misfit function to the time domain, Parseval's theorem and Inverse Fourier Transform are applied,

$$\begin{aligned}\delta\chi_{ij}^{dd}(T_{\max}) = 4\pi\int_0^{T_{max}} & F^{-1}\left\{W(\omega)\left[\Delta t_{ij}(\omega) - \Delta t_{ij}^{obs}(\omega)\right]p_{i|j}(\omega)\right\}\delta u_i(t)\,dt \\ & + F^{-1}\left\{W(\omega)\left[\Delta t_{ij}(\omega) - \Delta t_{ij}^{obs}(\omega)\right]p_{j|i}(\omega)\right\}\delta u_j(t)\,dt\end{aligned} \quad \text{(S7)}$$

where $p_{i|j}$ and $p_{j|i}$ are defined as,

$$\begin{aligned} p_{i|j}(\omega) &= \frac{i}{2\omega}\frac{1}{u_i(\omega)} = \frac{i}{2\omega}\frac{1}{A_i(\omega)}\frac{u_i^*(\omega)}{|u_i(\omega)|} \\ p_{j|i}(\omega) &= \frac{-i}{2\omega}\frac{1}{u_j(\omega)} = \frac{-i}{2\omega}\frac{1}{A_j(\omega)}\frac{u_j^*(\omega)}{|u_j(\omega)|}. \end{aligned} \quad \text{(S8)}$$

[0113] Eq. (S8) contains the complex conjugate phase factor of the synthetic waveform. Therefore, multi-taper analysis does not be applied for the synthetic waveform. An appropriate bandpass filter is used to remove the large amplitude in the transition band.

[0114] Based on Eqs. (S7 & S8), the adjoint sources for dispersive signals of one station triplet are defined as,

$$\begin{aligned} f_i^*(T-t) &= 4\pi F^{-1}\left\{W(\omega)\left[\Delta t_{ij}(\omega) - \Delta t_{ij}^{obs}(\omega)\right]p_{i|j}(\omega)\right\}(t)\,\delta(\mathbf{x}-\mathbf{x}_i) \\ f_j^*(T-t) &= 4\pi F^{-1}\left\{W(\omega)\left[\Delta t_{ij}(\omega) - \Delta t_{ij}^{obs}(\omega)\right]p_{j|i}(\omega)\right\}(t)\,\delta(\mathbf{x}-\mathbf{x}_j). \end{aligned} \quad \text{(S9)}$$

where the term T-t means time reversal of the right-hand side.

[0115] The backward (adjoint) wavefield is created by Eq.(S9), which defines the differential adjoint sources for differential time measurements on dispersive surface waves. Eq.(S8) defines some terms in Eq.(S9).

[0116] To sum the contributions from all triplets for one virtual source, it's more efficient to compute the combined sensitivity kernel using eq. (S10), which requires only one forward simulation and one adjoint simulation:

$$\chi^{dd} = \sum_{i,j \in \Omega} \chi_{ij}^{dd} , \qquad \text{(S10)}$$

where Ω contains the *i,j* pairs such that the distance 1-*j* is slightly longer than 1-*i* and they are in the (almost) same direction. Because of the linearity in eq. (S10), the adjoint sources of each station triplet are linearly added to corresponding stations.

[0117] Based on eq. (S1), the differential time structure kernel for one triplet is primarily sensitive to the velocity structure between the two nearby receivers. For the virtual source N101, the station triplet containing the receiver pair shows strong sensitivity between the two nearby receivers where differential time data are measured (FIG. 11A).

[0118] Similarly, strong structure sensitivity also concentrates between the receiver pair 25-27 (FIG. 11B) for the corresponding station triplet with larger station spacing.

[0119] The combined sensitivity kernel for the virtual source N101 (FIG. 11C) shows positive shear velocity sensitivity from near surface to ~3.5 km depth, suggesting that the actual shear velocity is slower than in the starting model. Moreover, the side lobes are significantly reduced due to the overlapping of multiple station triplets.

[0120] Ambient noise differential adjoint tomography is introduced to a linear array across the Los Angeles Basin (FIG. 12). The inverted shear-wave velocity model based on differential time measurements of Love wave phases reveals low-velocity zones (up to 50% reduction compared with the ray theory velocity model) corresponding to groundwater reservoirs from 200 m to 2 km depth that some deeper ones were not previously identified due to the limitation of borehole depth. Additionally, the inverted shear-wave velocity model in the top 100 m shows systematic agreements with the Vs 30 information from the independently derived geotechnical layer. Together, these results demonstrate the resolving power of the new differential adjoint tomography system compared with traditional ray theory tomography.

[0121] Ambient noise differential time adjoint tomography is applied to two different frequency bands: 1) low-frequency band 0.15-0.35 Hz, and 2) low+high-frequency band 0.15-1.5 Hz.

[0122] For the adjoint tomography at long periods (0.16-0.35 Hz), 36 stations are used as virtual sources to compute structure kernels, while 5 stations are used to prevent overfitting. In each iteration, the kernels and misfit values from different virtual sources are summed directly. Initially (FIG. 13), the sensitivity kernel of the 36 virtual sources shows strong positive sensitivity to low-velocity structures at shallow depths: up to 3.5 km SW of the Newport-Inglewood Fault and 2 km depth between the Newport-Inglewood Fault and Lower Elysian Park Thrust Fault. By the 13th iteration (FIG. 14), the sensitivity values are much smaller, and the positive and negative values may relate to residual data misfit near fault traces.

[0123] As the number of iterations increases, the total misfit decreases (FIG. 15), with optimization converging around the 14th iteration. However, validation using the 5 additional stations suggests that the minimum validation misfit occurs at the 13th iteration, and the 14th iteration increases the validation misfit, indicating overfitting. Thus, the inverted shear velocity model at the 13th iteration is chosen as the final result for the long period data.

[0124] Compared with the ray-theory-based initial shear velocity model (FIG. 16A), the low-frequency result (FIG. 16B) shows significant velocity reduction, with up to 50% velocity decrease at 300m depth and 23% decrease at 2km depth southwest of the Newport-Inglewood Fault. In addition, there are several shallow zones of substantial velocity reduction up to 30% located in between the local faults northeast of the Newport-Inglewood Fault, suggesting that the fault planes act as bi-material interfaces that separate geological units of different physical properties. The peak velocity reduction values for different shallow zones appear at ~300 m depth, suggesting sensitivity to layered structures at this depth.

[0125] Combining the low and high frequency differential time measurements, the final shear velocity model is obtained with an enhanced image at shallow depths of 0-800 m. The final velocity model shows only a marginal difference from the velocity model based on low-frequency Love wave data, suggesting that the low-frequency data are also sensitive to the shallow structure in the top 800 m in addition to the deeper structure between 800-3000 m depth.

[0126] To investigate the hydrological properties of the low-velocity layers, the Vp/Vs ratio is firstly estimated based on the adjoint shear velocity tomography result. The P wave velocity model is derived from the Long Beach nodal array using ambient seismic noise interferometry. For the overlapping part of the LASSIE and Long Beach nodal arrays, the Vp/Vs ratios are computed for the top 2 km of the sedimentary basin structure centered on the Newport-Inglewood Fault (FIG. 17 top). Apart from the shallow layer in the top 100 m, the Vp/Vs ratio reaches a peak value of 4.5 at X=2 km and 0.2-0.4 km depth southwest of the

Newport-Inglewood Fault, which correlates with a known aquifer – the Silverado aquifer according to the sequence stratigraphy from a well at Long Beach City College. Such large values are not unheard of, for example, similar and higher Vp/Vs ratios are found at Groningen, Netherlands in the top 0.2 km depth based on borehole seismic arrays. Previous surface wave tomography with long-period data using the regional broadband seismic network did not resolve the shallow layers in Los Angeles Basin where a high Vp/Vs ratio is found.

[0127] To convert the Vp/Vs ratio to porosity, the Biot-Gassmann Theory is adopted by Lee (BGTL) method, which models the pore fluid contribution to the Vp/Vs ratio for known rock frame properties. The lithology type is founded in the top 2 km depth is primarily sand/silt/clay near the LBCC borehole in the Long Beach area. For simplicity, it is assumed that the matrix material is half quartz and half clay in volume. In Table S1, the parameters are listed.

Parameter	Value
Shear modulus of quartz	45 Gpa
Bulk modulus of quartz	36 Gpa
Shear modulus of clay	6.85 Gpa
Bulk modulus of clay	20.9 Gpa
Density of quartz	2.65 g/cm^3

Table S1. Parameters used for converting Vp/Vs ratio to porosity using BGTL method.

[0128] Assuming the rock at shallow depth consists of 50% clay volume and 50% quartz, the estimated porosity at 0.8 km depth shows strong fluctuation between 0.25-0.38 (FIG. 17 bottom). At X= 2km, the porosity is 0.31 at 0.8 km depth, which is a local minimum. In contrast, the Vp/Vs ratio peaks at the same horizontal location between 0.2-0.4 km depth, indicating greater water saturation compared with other horizontal locations. These observations suggest that the sedimentary layer at 0.7-0.8 km depth is characterized by variable permeability, and the portion of the layer at X=2 km is less permeable than nearby segments, thereby storing more pore fluids at shallow depths between 0.2-0.6 km while reducing the porosity below 0.8 km depth.

[0129] The two blocks separated by the Newport Inglewood Fault show significant contrast in Vp/Vs ratio and porosity (FIG. 17), suggesting different materials for sedimentary layers across the fault interface. The sediments above 0.6 km depth in the NE block show lower Vp/Vs ratios than those from the SW block at the same depth range, indicating more pore fluids in the SW block at these shallow depths. For the sedimentary rocks situated below 0.7 km

depth, the NE block shows higher Vp/Vs ratios within 2 km from the fault interface than the SW block, suggesting higher porosity for the NE block at greater depths near the fault interface. This observation is clarified by converting the Vp/Vs ratio beneath 0.8 km depth to a lower-bound on porosity (FIG. 19), which shows the deep reservoirs have porosity around 0.33.

[0130] The porosity information is directly related to Vp/Vs ratios, but the P-wave velocity model is only available in the top 2 km and spans 10 km away from the Newport-Inglewood Fault due to the limitation of the Long Beach array [15]. Therefore, our study of porosity is limited to the smaller volume where both Vp and Vs models overlap. Another limitation is that the BGTL method only works for a depth range where the differential pressure is ~ 15 MPa. The *P*-wave velocity beneath Long Beach, however, contains much less lateral variation than the S-wave velocity. Therefore, most of the observed lateral variations in Vp/Vs ratio arise from the S-wave velocity model, which is more sensitive to pore fluids in sedimentary rocks than the P-wave model. Assuming the differential pressure is similar at the same depth, the first limitation can be alleviated by comparing the lateral variation of shear velocity update after adjoint tomography (e.g. FIG. 16B & C), as the shear velocity reduction indicates larger Vp/Vs ratio and therefore higher porosity. The second limitation can be reduced by estimating the lower bound of porosity for deeper depths with higher differential pressure (e.g. FIG. 19).

[0131] The estimated shallow shear-wave velocity structure is compared with the Vs 30 data from the geotechnical layer beneath the LASSIE array (FIG. 18). The inverted shear- wave velocity is derived from the top 100 m due to the limitation of the grid size in adjoint tomography. The geotechnical layer was sparsely sampled (by strong motion stations) and Vs 30 values are grouped by different geological units.

[0132] The inverted shear wave velocity in top 100 m (Vs 100) from adjoint tomography is considerably lower than that from ray theory tomography (FIG. 18). The trend of Vs 100 generally increases as the distance from the coast increases. For adjoint tomography, the Vs 100 SW of the Newport-Inglewood Fault is the lowest, which is close the Vs 30 values from the geotechnical layer. For the block NE of Newport-Inglewood Fault, Vs 100 is higher while the Vs 30 shows decreasing velocity.

[0133] For the geological unit between the Los Alamitos Fault and the Lower Elysian Park Thrust Fault, both the inverted Vs 100 (adjoint tomography) and the Vs 30 decrease at the edges of the unit. Vs 30 remains constant within the geological unit – perhaps due to sparse sampling, while Vs 100 exhibits lateral variations within the unit and is almost twice the value of Vs 30.

[0134] The high topography above the Whittier Fault corresponds to higher Vs 100 and Vs 30, while the inverted Vs 100 is ~0.15 km/s faster than Vs 30. In this case, the inverted Vs 100 from adjoint tomography matches the trend of the ray theory Vs 100, but is slightly lower.

[0135] Ambient noise differential adjoint tomography shows great potential for resolving detailed geological/hydrological structures in urban sedimentary basins. It reduces the bias caused by uneven and temporally variable noise source distribution. Moreover, to address the overfitting problem in the optimization step, 5 stations are used as virtual sources for a validation dataset, which is independent from the training dataset consisting of 36 virtual sources. By minimizing the validation error, the optimal velocity model is chosen that do not overfit to the training dataset. This approach is widely used in machine learning and could be useful for adjoint tomography community. It is similar to cross validation, but the multiple different combinations of training and validation sets required for true cross validation are not feasible due to the computational demands of adjoint tomography.

[0136] The Vp and Vs models are derived from different seismic arrays with different approaches. The Vp model is based on P-wave phases extracted from the noise interferometry data of the 2D Long Beach nodal array through ray tracing of refracted P wave ray paths. The Vs model derived here is from the ambient noise differential adjoint tomography based on wave equations and a linear array. Therefore, it's possible that some unresolved P-wave velocity variations may be missing in the Vp/Vs ratio (FIG. 19). Due to the density of Long Beach nodal array and the proximity to the coast, however, the unresolved low-Vp anomaly at the shallow depths (top 1 km) is unlikely to be as significant as the Vs anomaly.

[0137] The spatial distribution of porosity and its lower bound have important implications for hydrological studies in the Long Beach sedimentary basin. The higher porosity directly correlates with greater S-wave velocity reduction, which allows us to use the S-wave velocity model anomaly (FIG. 16C) to predict relative fluid abundance at the same depth for a broader cross-section from Long Beach to Anaheim (X from 0 to 20 km). These results suggest that the Silverado aquifer at 0.2-0.4km depth has spatially variable pore fluids, and the water-bearing reservoirs at different depths can be interconnected by vertical channels with higher permeability than surrounding rocks. The abundant fluids around the Newport-Inglewood fault suggest vertical migration of water from surface to aquifers at different depths, which provides a means of fluid replenishment for the Silverado aquifer. Based on the spatial variation of pore fluids derived from tomography, future study of both horizontal and vertical fluid migration patterns can help achieve sustainable groundwater extraction and avoid drilling unnecessary

water wells in general, and in Los Angeles or other big cities in particular. Ambient noise differential adjoint tomography is therefore a cost-effective way of identifying aquifers and locations with higher fluid content, optimizing the drilling of new water wells and helping to provide access to freshwater for big cities.

[0138] Moreover, the existence of abundant pore fluids around the Newport-Inglewood Fault coincides with the higher seismicity in the top 5 km on the same fault observed by the Long Beach phase B array to the south the LASSIE array, possibly because the higher porosity reduces the effective normal stress on the fault plane, increasing the microseismicity. This is analogous to induced earthquakes and some natural earthquakes in southern California being induced by fluid pressure variations.

[0139] **In addition, the system of an embodiment of the present invention method is applied to a marine acquisition for a linear OBS array off Kumano**, Kii peninsula, Japan (FIG. 20).

[0140] The resulting S-wave velocity model (FIG. 21) reveals significantly low S-wave velocity in the southwestern part of the Kumano Basin and the incoming sediments above the subducting oceanic crust of the Philippine Sea Plate. Specifically, in the southwestern portion of the Kumano Basin beneath the linear array (for X between 65-85 km), the S-wave velocities are low, ranging between 0.2-0.5 km/s in the top 3 km depth, forming a distinctive bowl-shaped structure. For comparison, this bowl-shaped structure corresponds to approximately 40-60% velocity reduction with respect to the surrounding rocks. The southern Kumano Basin is interpreted as a fluid-rich sedimentary basin compared with the northern Kumano Basin, which agrees with the spatial distribution of slow earthquakes between OBS74 and OBS79 (FIG. 20) that requires abundant fluids at the subducting plate interface. The fluids at plate interface are believed to be the source of fluids in southern Kumano Basin.

[0141] Overlaying the S-wave velocity model with the migrated seismic reflection profile from MCS (Multi-Channel Seismic) dataset, we find striking agreements between the low-velocity region in southwestern Kumano Basin and seismic reflectors outlining the shape and sedimentary layers of the basin (FIG. 21). In addition, the low-velocity incoming sediment (X between 20-30 km) south of the deformation front correlates with the sedimentary layer reflections in MCS seismic profile.

[0142] In summary, in the embodiments of the present invention, the main function includes:

[0143] A linear triplet of stations array with one virtual source and two closely positioned receivers of seismic signal;

[0144] Using the seismic noise received from 3 stations to compute noise interferometry;

[0145] Generating differential adjoint tomography based on surface wave from noise interferometry;

[0146] Estimating the shear wave velocity from adjoint tomography;

[0147] Using the estimated tomography to estimate the actual underground geophysical/hydrological properties e.g. underground fluid reservoirs can be located.

[0148] In some embodiments, the processor executives the following steps:

[0149] replacing the virtual source with a point source to generate dispersive surface wave signals.

[0150] In some embodiments, the spacing between receivers should be small, i.e. the distance between source and the receiver positioned farther should be less than 125% of the distance between source and receiver positioned closer. The angle between straight lines connecting the source and every receiver should be less than 5 degrees.

[0151] In some embodiments, the processer use the differential time measurements for the noise interferometric function to create a misfit function for dispersive surface wave signals.

[0152] In some embodiments, the processor use elastic wave equation to compute gradient of differential-time misfit function.

[0153] In some embodiments of the present invention, by replacing the virtual source with a point source, the differential-time kernels (gradients) are similar to those before replacement. The processor of the system greatly simplifies the calculations through this approach, and the linear array formed by the seismic wave recording devices can provide proper ambient noise differential adjoint tomography.

[0154] In some embodiments of the present invention, the processor of the system uses differential travel time to compute kernels, and the processor reduces sensitivity to noise sources with this approach.

[0155] In some embodiments of the present invention, the processor of the system defines the differential-time adjoint sources for ambient noise differential adjoint tomography.

[0156] In some embodiments of the present invention, the processor of the system uses differential time misfit function.

[0157] In some embodiments of the present invention, the processor of the system executive the following steps:

[0158] a) Compute seismic noise interferometry for two station pairs: 1-2. 1-3, where 1 denotes virtual source. 2 and 3 are receivers. The noise interferometries includes noise interferometric functions.

[0159] b) Measure the observed differential time for dispersive surface wave signals from the noise interferometric functions 1-2, 1-3. (Eq. 1)

[0160] c) Replace the virtual source by a point source. Model the synthetic surface wave signals from the point source. Compute the synthetic (modeled) differential time. (Eq.1)

[0161] d) Define the misfit function (Eq.1) for one triplet as a squared sum of differences between observed and synthetic differential time at different frequencies due to dispersion. (Dispersion: seismic surface wave travels at different speed for different frequency)

[0162] e) Compute the gradient (2*) (Eq.4) of misfit function by forward (wave equation-based) wave propagation from the point source and the backward wave propagation from the receivers.

[0163] f) To generate backward surface wave propagation from the receivers, the differential adjoint sources of dispersive surface wave signals are defined (Eq. S7,S8,S9). Optionally, some technique for spectral density estimation (e.g. Welch's method, Multitaper) can be added to Eq. S9.

[0164] g) For each virtual source, sum over all eligible station triplets (Eq. S10) to produce the misfit and gradient (sensitivity) of one virtual source (Fig. 11C).

[0165] h) Sum over all virtual sources to produce a combined gradient (Fig. 13&14, structure sensitivity).

[0166] i) Use the combined gradient to update the shear wave velocity model iteratively (Fig. 15). This process is called differential adjoint tomography.

[0167] j) Obtain the S wave velocity model after adjoint tomography (Fig. 5).

[0168] The processor derives shear modulus (= shear rigidity) directly from shear wave velocity by assuming density values.

[0169] Gradient is the spatial derivative of the misfit function with respect to the parameter (e.g. shear wave velocity).

[0170] The functional units and modules of an ambient noise differential adjoint tomography system in accordance with the embodiments disclosed herein may be implemented using computing devices, computer processors, or electronic circuitries including but not limited to application specific integrated circuits (ASIC), field programmable gate arrays (FPGA), microcontrollers, and other programmable logic devices configured or programmed according to the teachings of the present disclosure. Computer instructions or software codes running in the computing devices, computer processors, or programmable logic devices can readily be prepared by practitioners skilled in the software or electronic art based on the teachings of the present disclosure.

[0171] All or portions of the methods in accordance to the embodiments may be executed in one or more computing devices including server computers, personal computers, laptop computers, mobile computing devices such as smartphones and tablet computers.

[0172] The embodiments may include computer storage media, transient and non-transient memory devices having computer instructions or software codes stored therein, which can be used to program or configure the computing devices, computer processors, or electronic circuitries to perform any of the processes of the present invention. The storage media, transient and non-transient memory devices can include, but are not limited to, floppy disks, optical discs, Blu-ray Disc, DVD, CD-ROMs, and magneto-optical disks, ROMs, RAMs, flash memory devices, or any type of media or devices suitable for storing instructions, codes, and/or data.

[0173] Each of the functional units and modules in accordance with various embodiments also may be implemented in distributed computing environments and/or Cloud computing environments, wherein the whole or portions of machine instructions are executed in distributed fashion by one or more processing devices interconnected by a communication network, such as an intranet, Wide Area Network (WAN), Local Area Network (LAN), the Internet, and other forms of data transmission medium.

[0174] The foregoing description of the present invention has been provided for the purposes of illustration and description. It is not intended to be exhaustive or to limit the invention to the precise forms disclosed. Many modifications and variations will be apparent to the practitioner skilled in the art.

[0175] The embodiments were chosen and described in order to best explain the principles of the invention and its practical application, thereby enabling others skilled in the art to understand the invention for various embodiments and with various modifications that are suited to the particular use contemplated.

CLAIMS

What is claimed is:

1. An ambient noise differential adjoint tomography system, comprising:
a plurality of seismic wave recording devices, disposed on a region; and
a processor, connecting the seismic wave recording devices,
wherein the processor indicates three of the seismic wave recording devices as a source, a first receiver, and a second receiver, and the source and the first and second receivers are arranged as a linear array, and the first and second receivers are positioned nearby each other,
wherein the processor receives seismic noise from the source, the first receiver, and the second receiver and obtain a noise interferometry,
wherein the processor compute synthetic dispersive surface wave signals with the source and the first and second receivers,
wherein the processor generates a differential adjoint tomography based on observed dispersive surface wave from the noise interferometry,
wherein the processor estimates a shear wave velocity from the differential adjoint tomography,
wherein the processor uses the estimated tomography to estimate the characteristic of the region, and the processor provide a diagram with characteristic of the region through a display or printer.

2. The system of claim 1, wherein a first distance is between the first and second receivers, and a second distance is the minimal distance between the source and one of the first and second receivers, and a ratio of the first and second distances ranges from 1% to 30%.

3. The system of claim 1, wherein a first reference line is a straight line connecting the source and the first receiver, and a second reference line is a straight line connecting the source and the second receiver, and an included angle included by the first reference line and the second reference line is less than 5 degrees.

4. The system of claim 1, wherein a third distance is between the source and the first receiver, and a fourth distance is between the source and the second receiver, and the fourth distance is less than 1.25 times of the third distance.

5. The system of claim 1, wherein the characteristic comprises actual underground geophysical property or hydrological property of the region.

6. The system of claim 1, wherein the seismic wave recording devices comprise more than 30 seismographs, and the seismographs are deployed across the Los Angeles Basin.

7. The system of claim 1, wherein the seismic wave recording devices form a linear ocean bottom seismometer (OBS) array, and the OBS array is deployed across the Nankai Trough off the Kii Peninsula, Japan.

8. An ambient noise differential adjoint tomography system, comprising:
a plurality of seismic wave recording devices, disposed on a region; and
a processor, connecting the seismic wave recording devices
wherein the processor indicates three of the seismic wave recording devices as a source, a first receiver, and a second receiver, and the first and second receivers are disposed nearby while each of them have different distance measuring from the source, and the source is disposed far away from the receivers, and the source and the receivers are linearly disposed,
wherein the source and the receivers record ambient noise and generate ambient noise data,
wherein the processor compute a seismic noise interferometry by cross-correlating the ambient noise data from the source and the receivers to generate virtual earthquake signals,
wherein the processor measures the observed differential times between the virtual earthquake signals for receivers at different frequencies,
wherein the processor creates an initial S wave velocity model based on existing information or assumptions,
wherein the processor simulates synthetic waveforms using the initial velocity model and compute the corresponding synthetic differential times,
wherein the processor calculates the misfit between the observed and synthetic differential times,
wherein the processor compute the gradient of the misfit function using the adjoint method, which involves simulating the forward and backward propagation of seismic waves,
wherein the processor updates the S wave velocity model iteratively by minimizing the misfit between the observed and synthetic differential times,
wherein the processor repeates the steps above until the misfit is sufficiently small or a desired level of convergence is achieved,

wherein the processor obtain the final S wave velocity model that best explains the observed differential times, and the processor present the S wave velocity model in diagrams with a display or printer.

9. The system of claim 8, wherein a first distance is between the first and second receivers, and a second distance is the minimal distance between the source and one of the first and second receivers, and a ratio of the first and second distances ranges from 1% to 30%.

10. The system of claim 8, wherein a first reference line is a straight line connecting the source and the first receiver, and a second reference line is a straight line connecting the source and the second receiver, and an included angle included by the first reference line and the second reference line is less than 5 degrees.

11. The system of claim 8, wherein a third distance is between the source and the first receiver, and a fourth distance is between the source and the second receiver, and the fourth distance is less than 1.25 times of the third distance.

12. The system of claim 8, wherein the characteristic comprises actual underground geophysical property or hydrological property of the region.

13. The system of claim 8, wherein the seismic wave recording devices comprise more than 30 seismographs, and the seismographs are deployed across the Los Angeles Basin.

14. The system of claim 8, wherein the seismic wave recording devices form a linear ocean bottom seismometer (OBS) array, and the OBS array is deployed across the Nankai Trough off the Kii Peninsula, Japan.

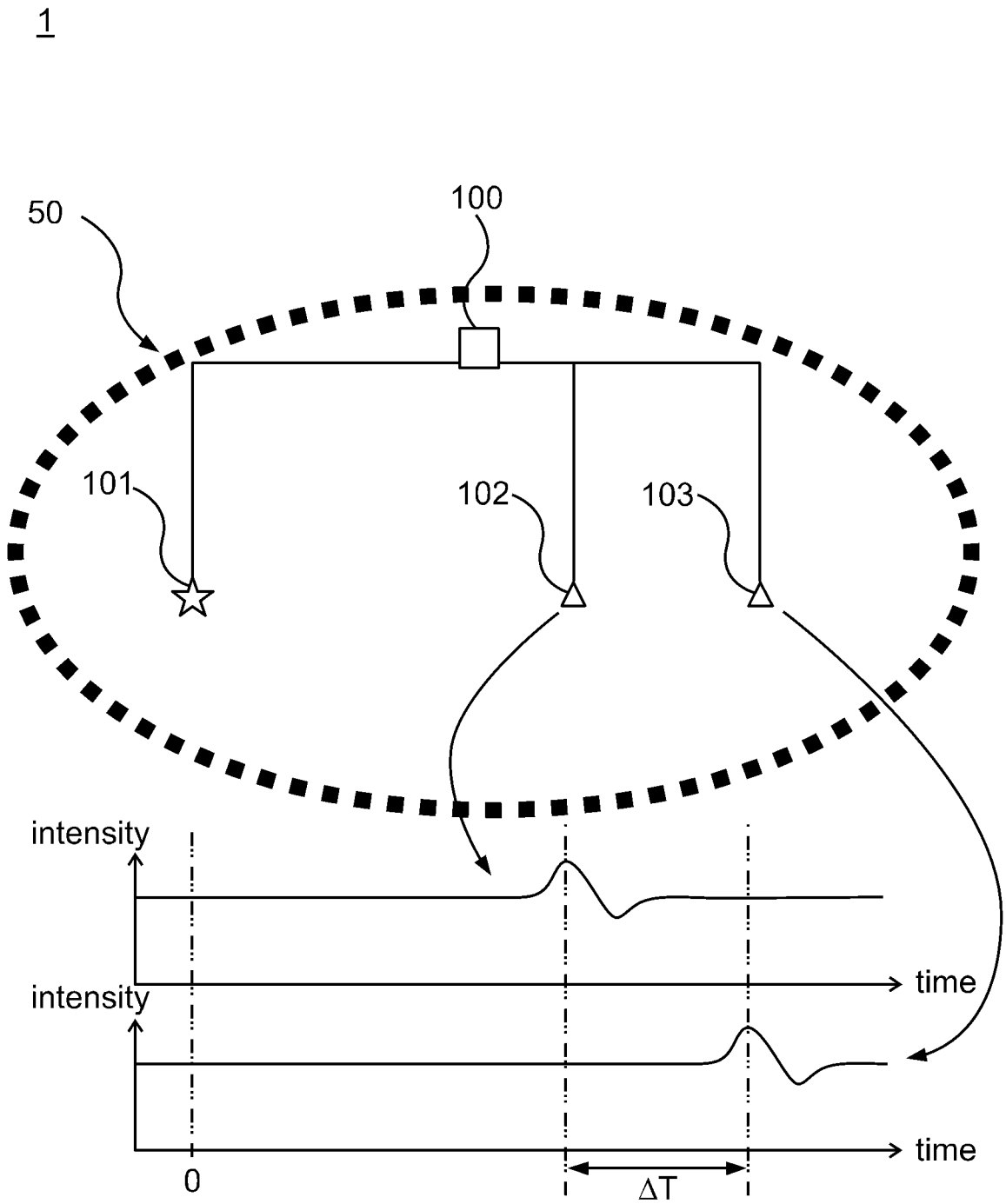

FIG. 1

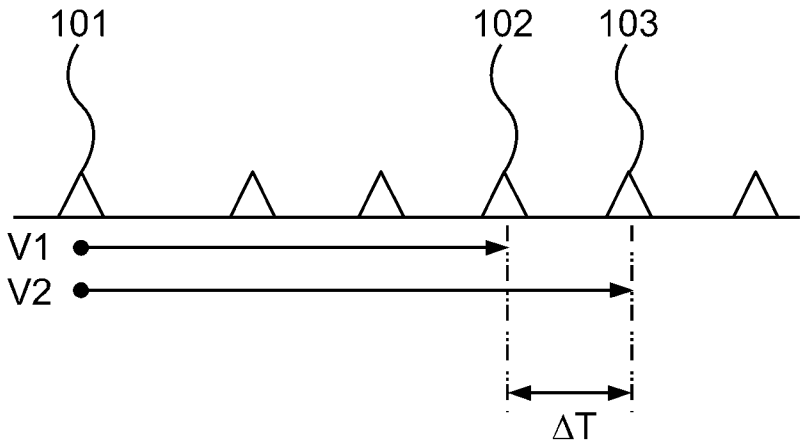

FIG. 2

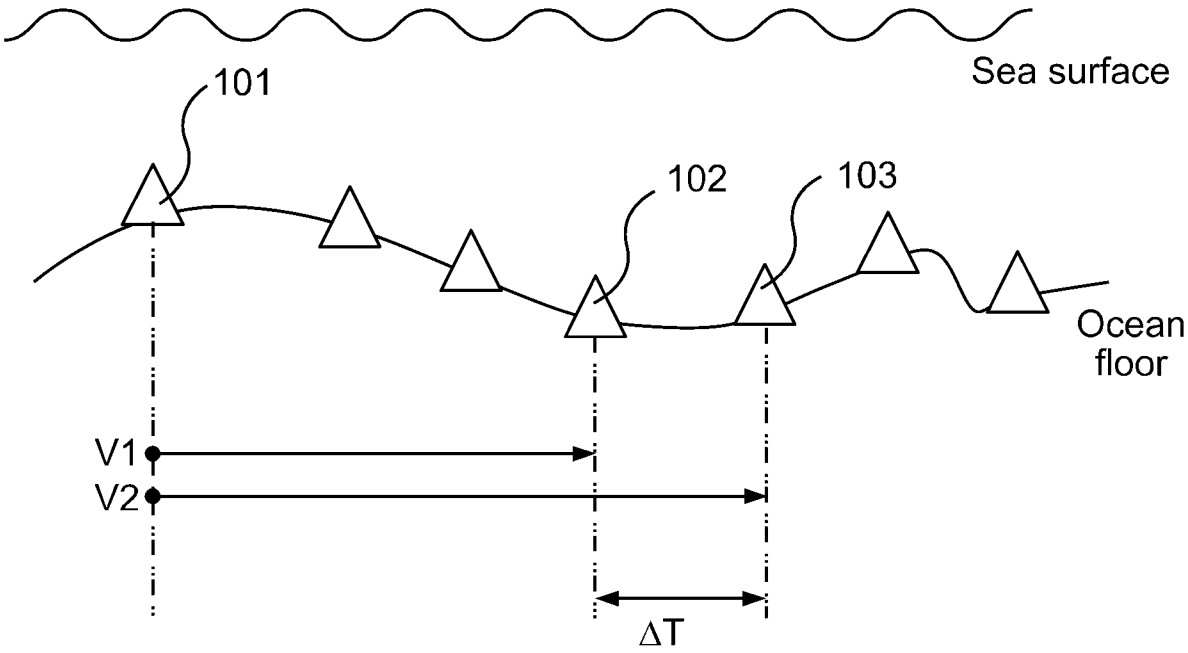

FIG. 3

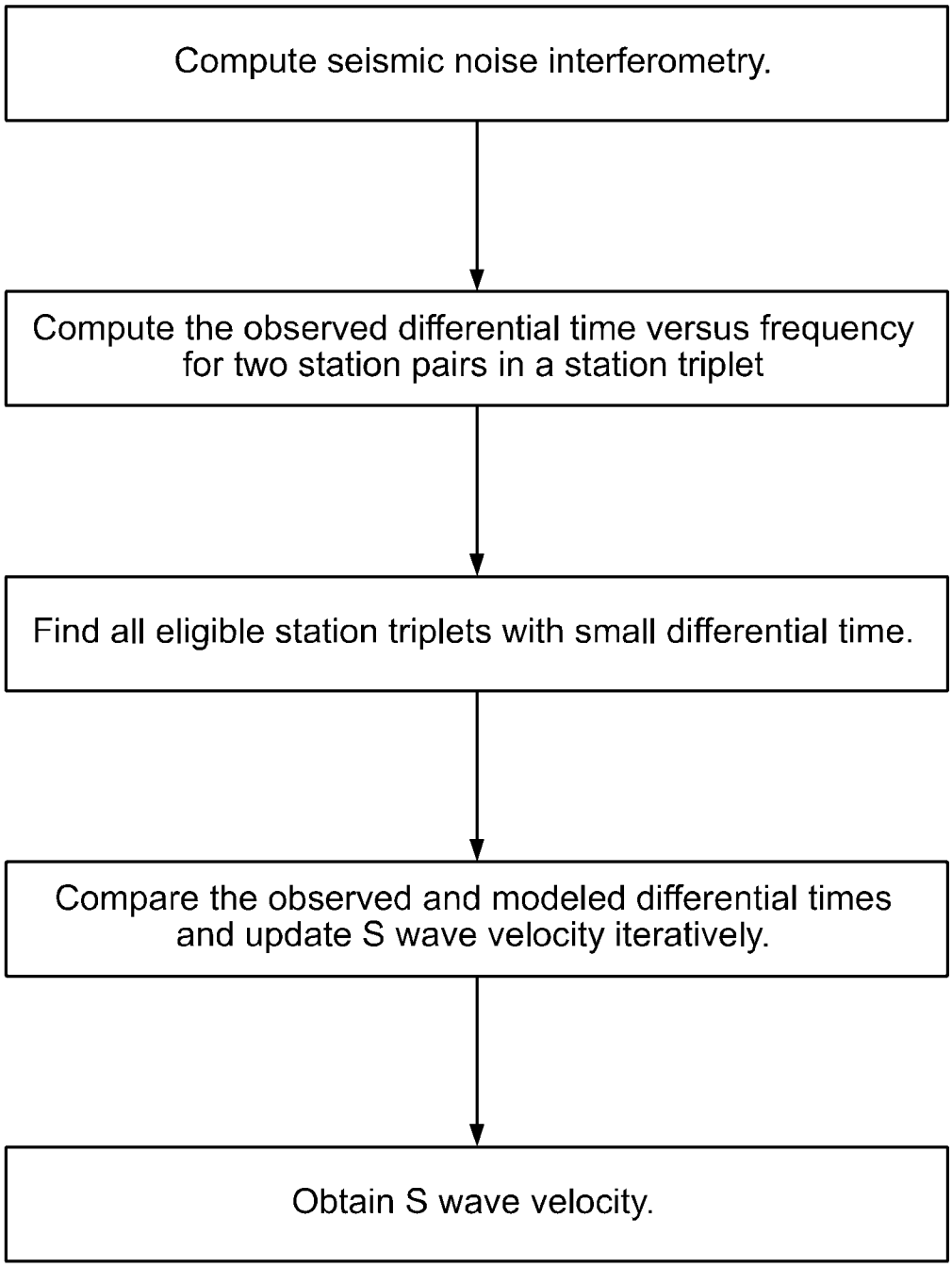
Compute seismic noise interferometry.
Compute the observed differential time versus frequency for two station pairs in a station triplet
Find all eligible station triplets with small differential time.
Compare the observed and modeled differential times and update S wave velocity iteratively.
Obtain S wave velocity.

FIG. 4

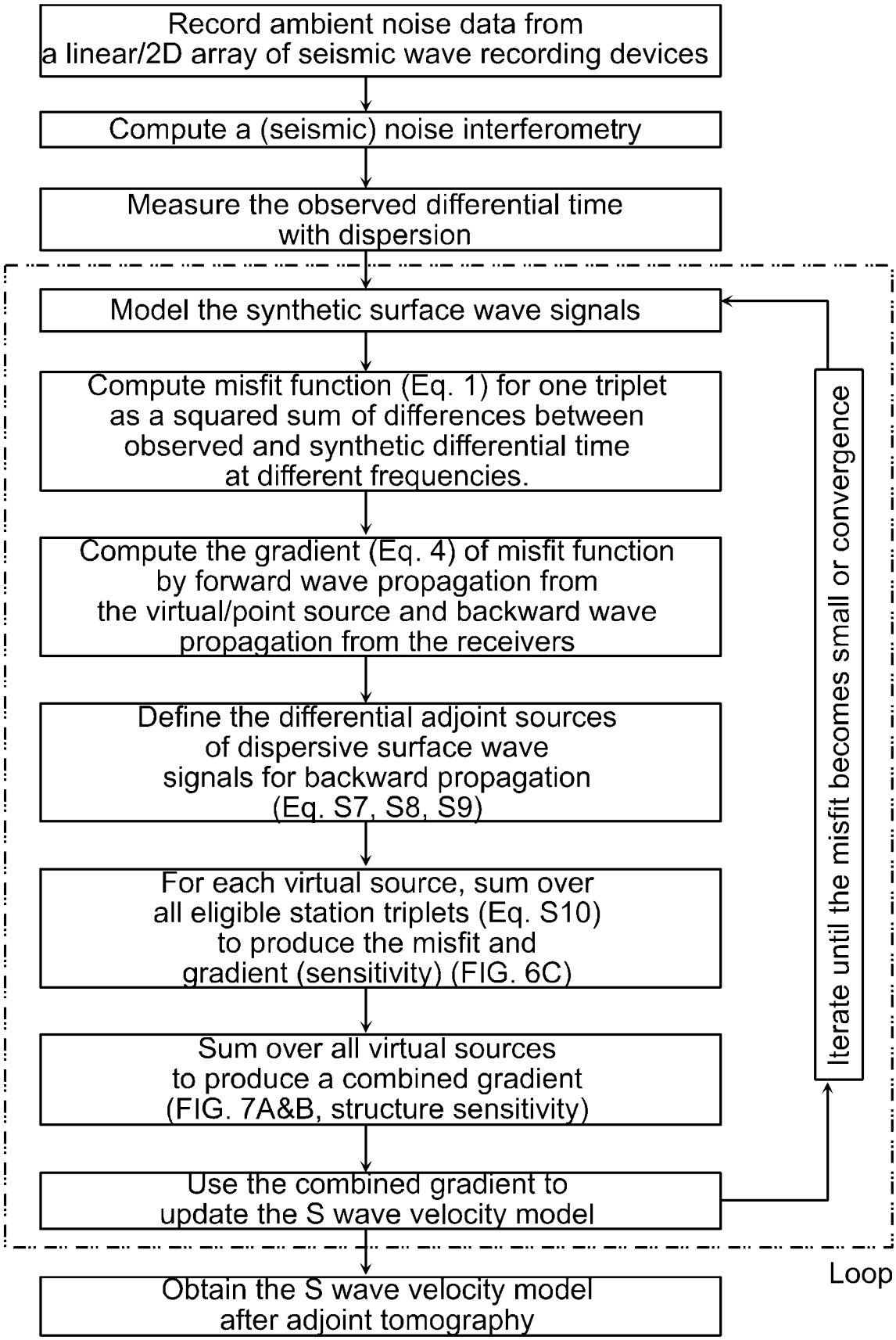
Record ambient noise data from a linear/2D array of seismic wave recording devices
Compute a (seismic) noise interferometry
Measure the observed differential time with dispersion
Model the synthetic surface wave signals
Compute misfit function (Eq. 1) for one triplet as a squared sum of differences between observed and synthetic differential time at different frequencies.
Compute the gradient (Eq. 4) of misfit function by forward wave propagation from the virtual/point source and backward wave propagation from the receivers
Define the differential adjoint sources of dispersive surface wave signals for backward propagation (Eq. S7, S8, S9)
For each virtual source, sum over all eligible station triplets (Eq. S10) to produce the misfit and gradient (sensitivity) (FIG. 6C)
Sum over all virtual sources to produce a combined gradient (FIG. 7A&B, structure sensitivity)
Use the combined gradient to update the S wave velocity model
Iterate until the misfit becomes small or convergence
Loop
Obtain the S wave velocity model after adjoint tomography

FIG. 5

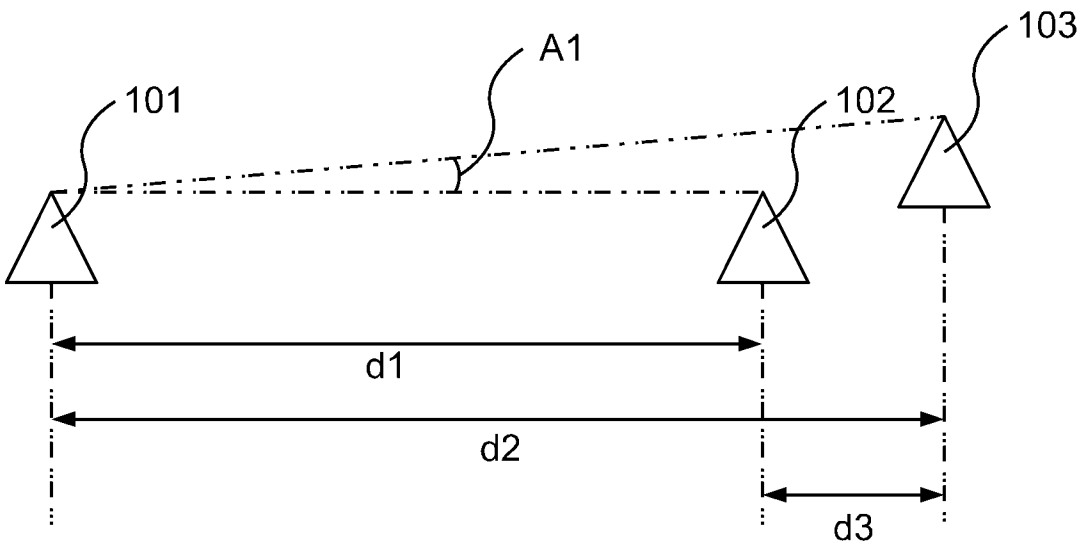

FIG. 6

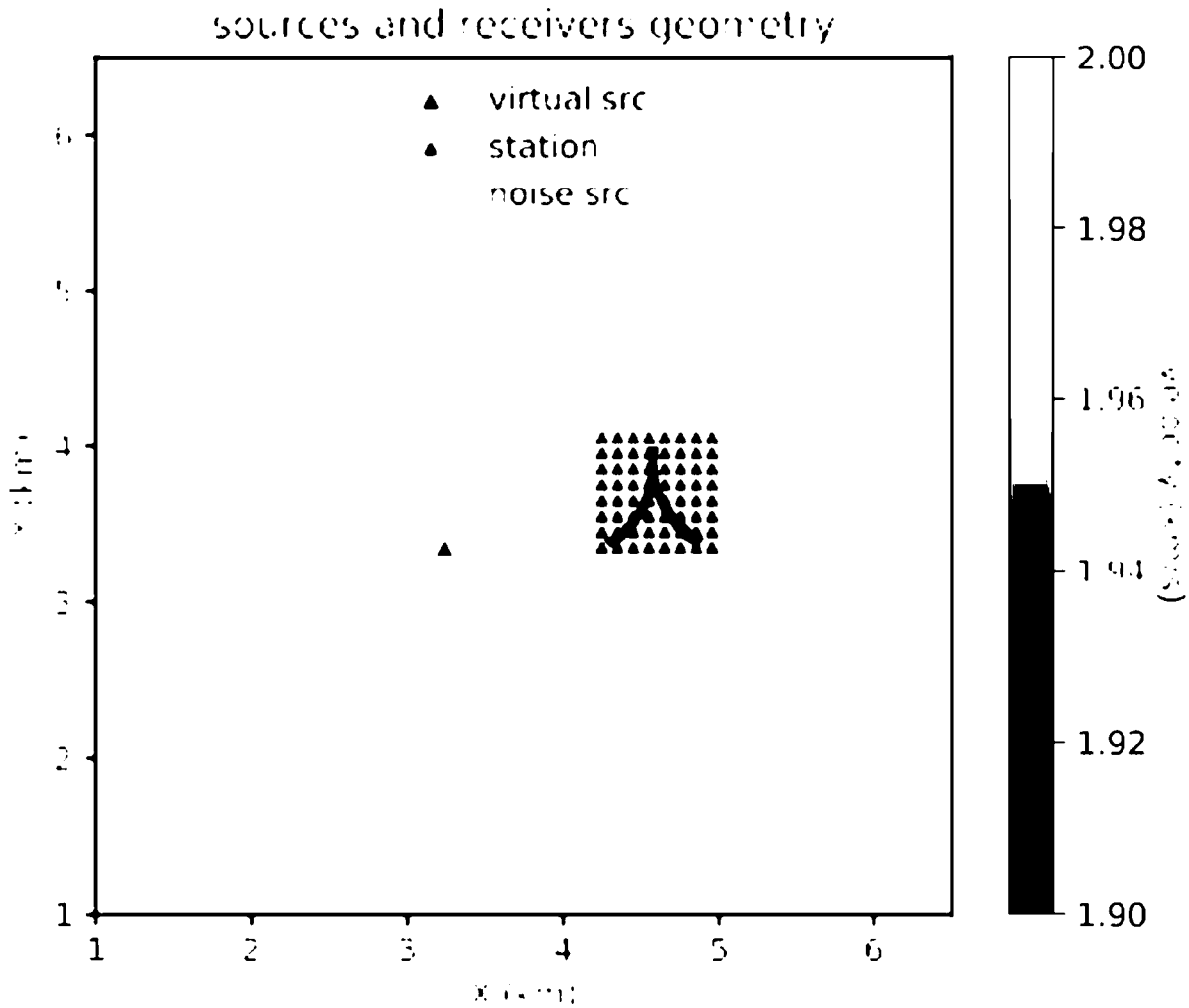
sources and receivers geometry
virtual src
station
noise src
1
2
3
4
5
6
2.00
1.98
1.96
1.94
1.92
1.90

FIG. 7

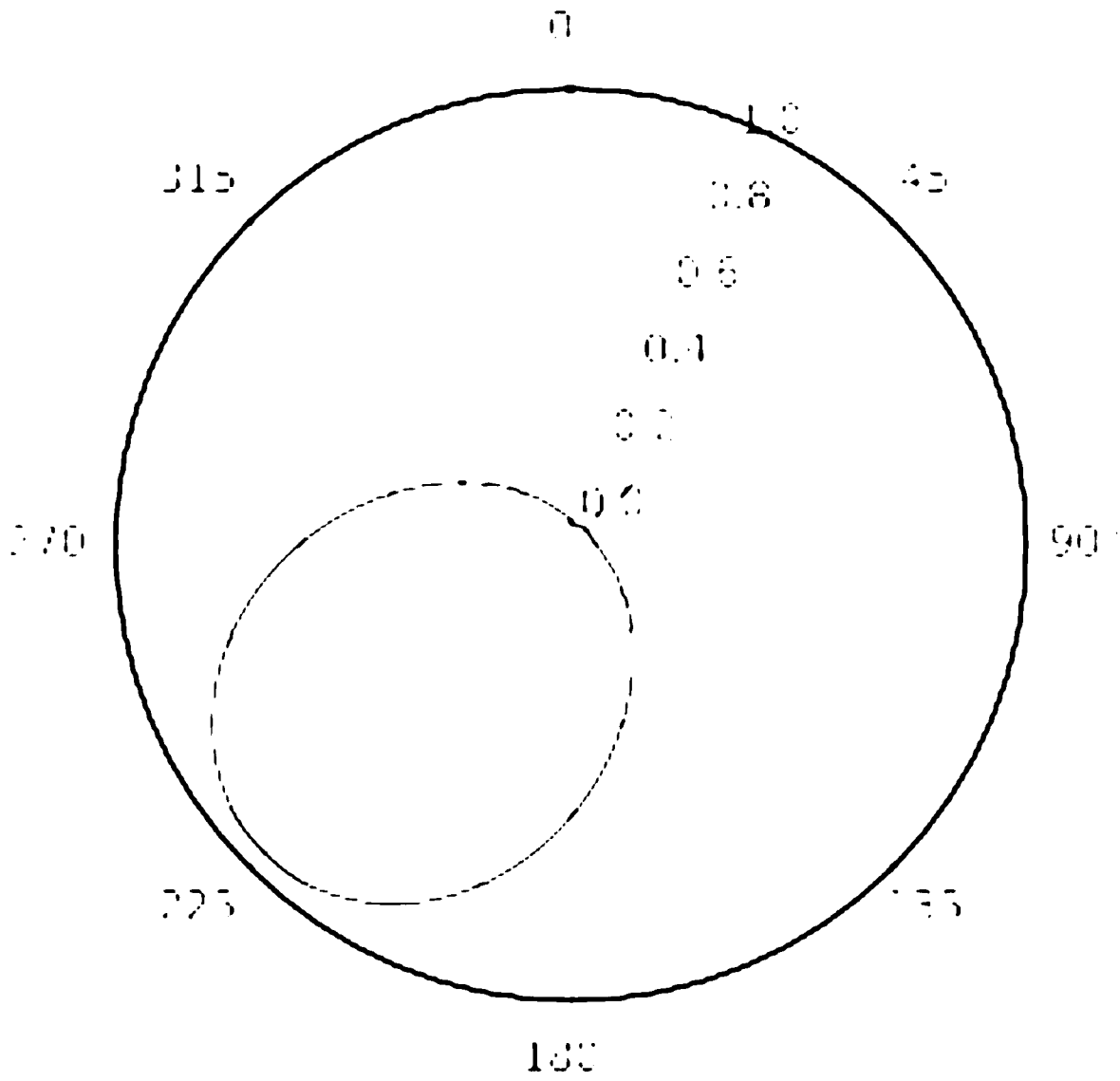

FIG. 8

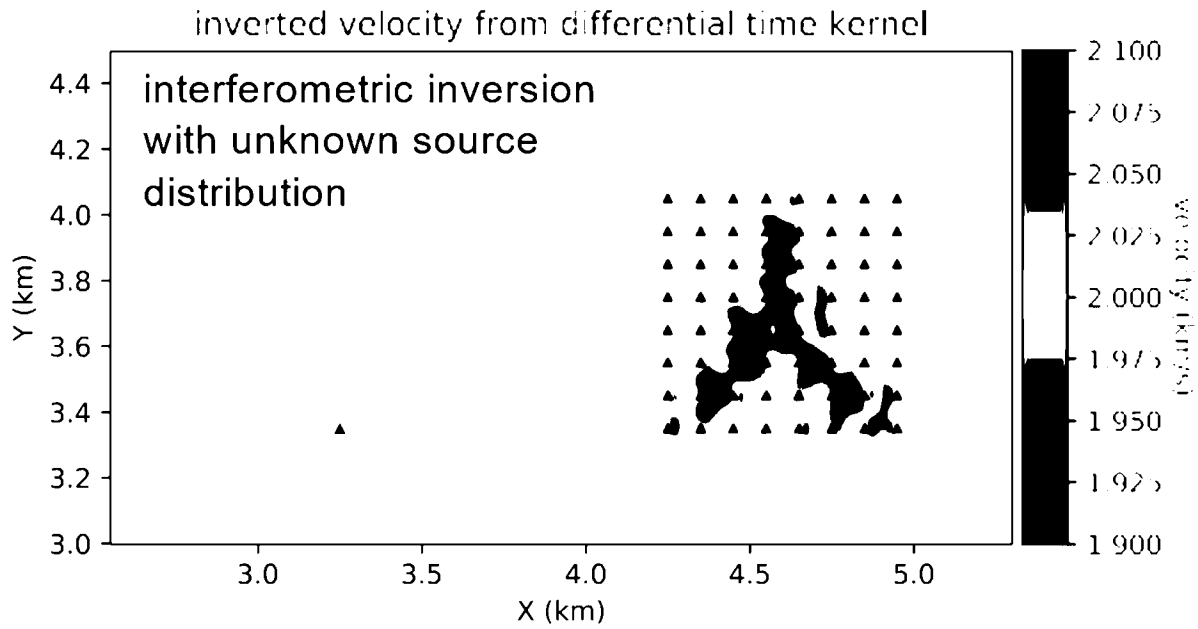
inverted velocity from differential time kernel
interferometric inversion
with unknown source
distribution
Y (km)
X (km)
4.4
4.2
4.0
3.8
3.6
3.4
3.2
3.0
3.0
3.5
4.0
4.5
5.0
2 100
2 075
2 050
2 025
2 000
1 975
1 950
1 925
1 900

FIG. 9

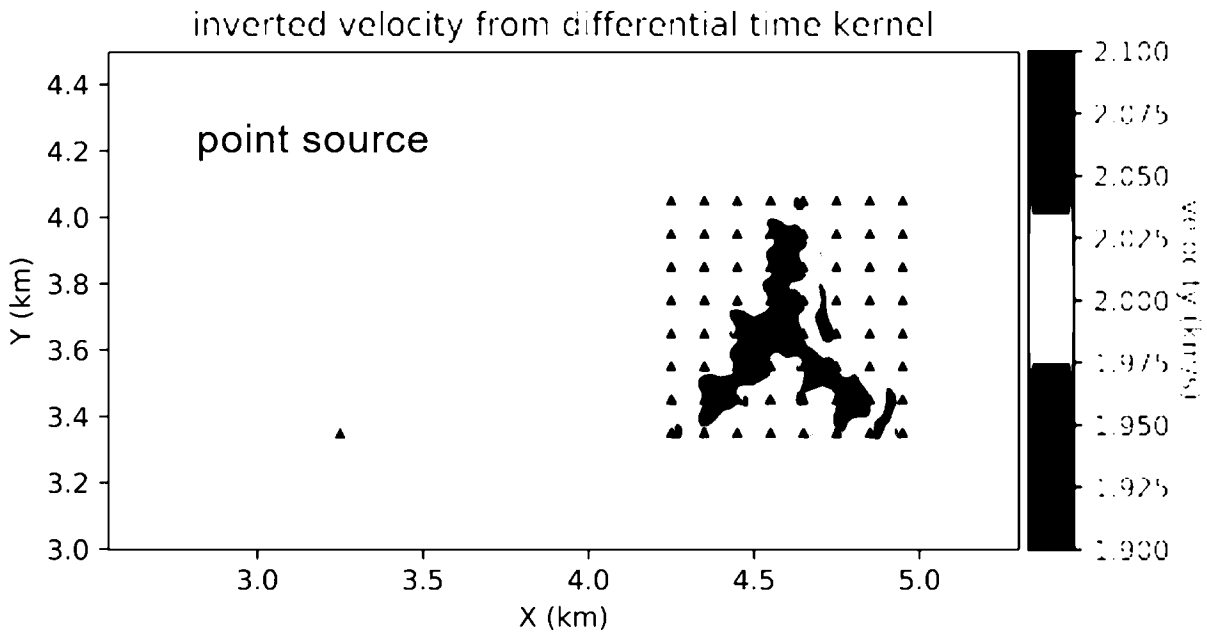
inverted velocity from differential time kernel
point source
Y (km)
X (km)
4.4
4.2
4.0
3.8
3.6
3.4
3.2
3.0
3.0
3.5
4.0
4.5
5.0
2.100
2.075
2.050
2.025
2.000
1.975
1.950
1.925
1.900

FIG. 10

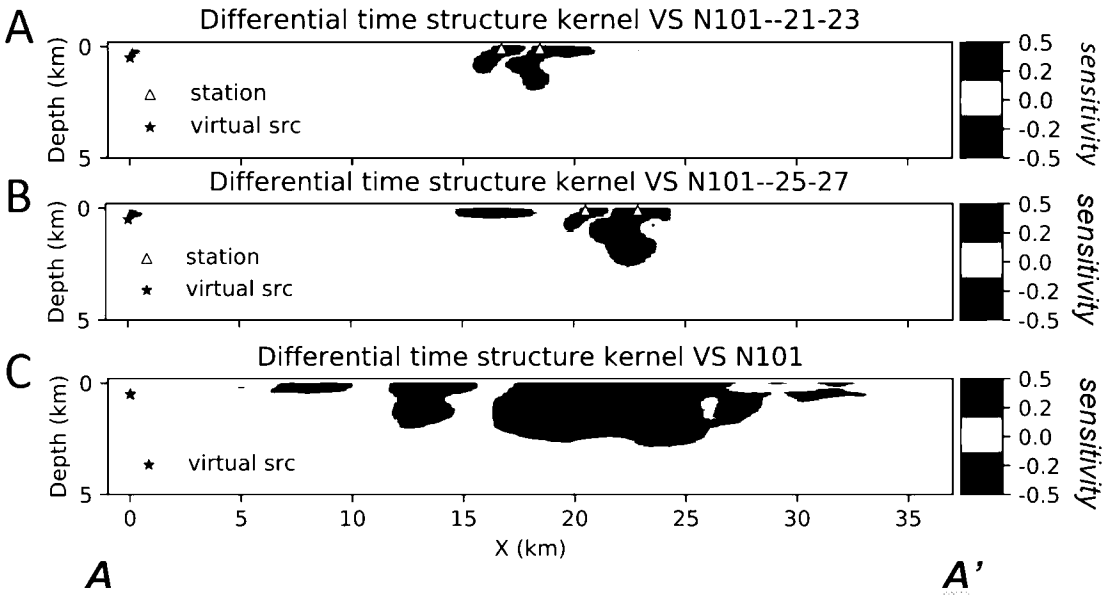
A
Differential time structure kernel VS N101--21-23
Depth (km)
0
5
station
virtual src
0.5
0.2
0.0
-0.2
-0.5
sensitivity
B
Differential time structure kernel VS N101--25-27
Depth (km)
0
5
station
virtual src
0.5
0.2
0.0
-0.2
-0.5
sensitivity
C
Differential time structure kernel VS N101
Depth (km)
0
5
virtual src
0.5
0.2
0.0
-0.2
-0.5
sensitivity
0
5
10
15
20
25
30
35
X (km)
A
A'

FIG. 11

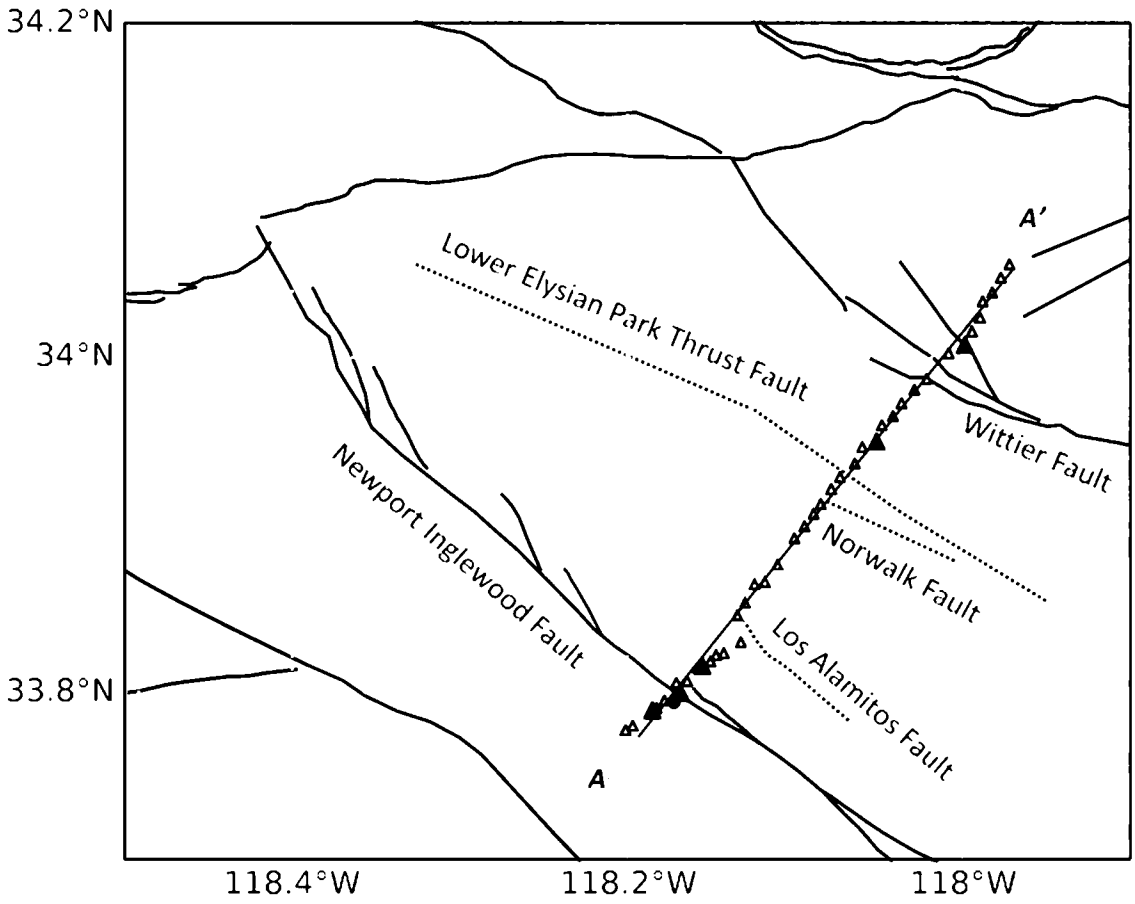
34.2°N
34°N
33.8°N
118.4°W
118.2°W
118°W
A'
A
Lower Elysian Park Thrust Fault
Wittier Fault
Norwalk Fault
Los Alamitos Fault
Newport Inglewood Fault

FIG. 12

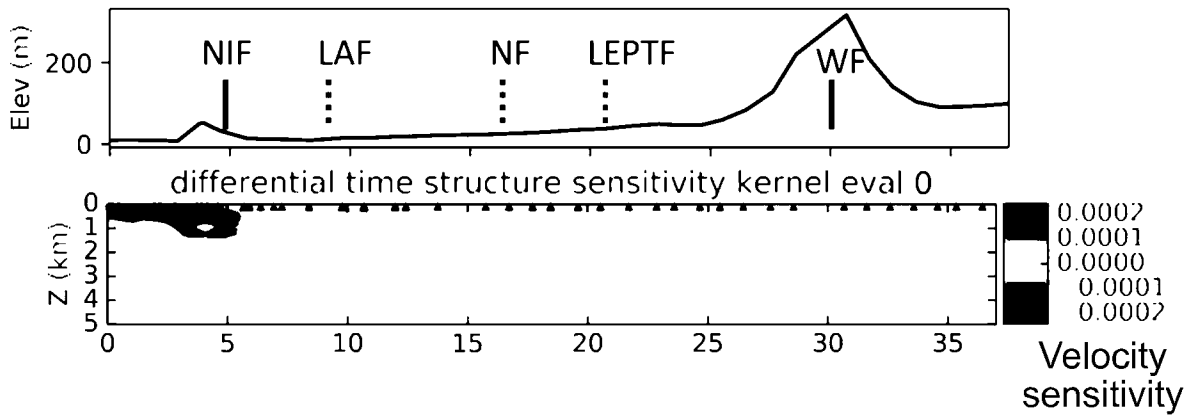
Elev (m)
200
0
NIF
LAF
NF
LEPTF
WF
differential time structure sensitivity kernel eval 0
Z (km)
0
1
2
3
4
5
0
5
10
15
20
25
30
35
0.0002
0.0001
0.0000
0.0001
0.0002
Velocity
sensitivity

FIG. 13

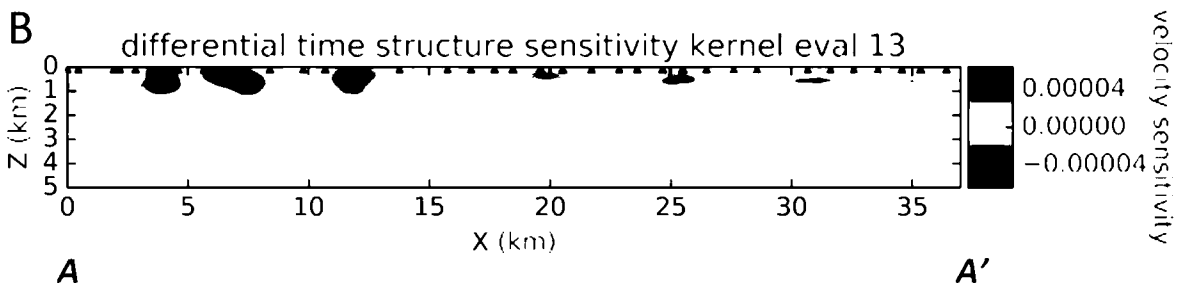
B
differential time structure sensitivity kernel eval 13
Z (km)
0
1
2
3
4
5
0
5
10
15
20
25
30
35
X (km)
A
A′
0.00004
0.00000
−0.00004
velocity sensitivity

FIG. 14

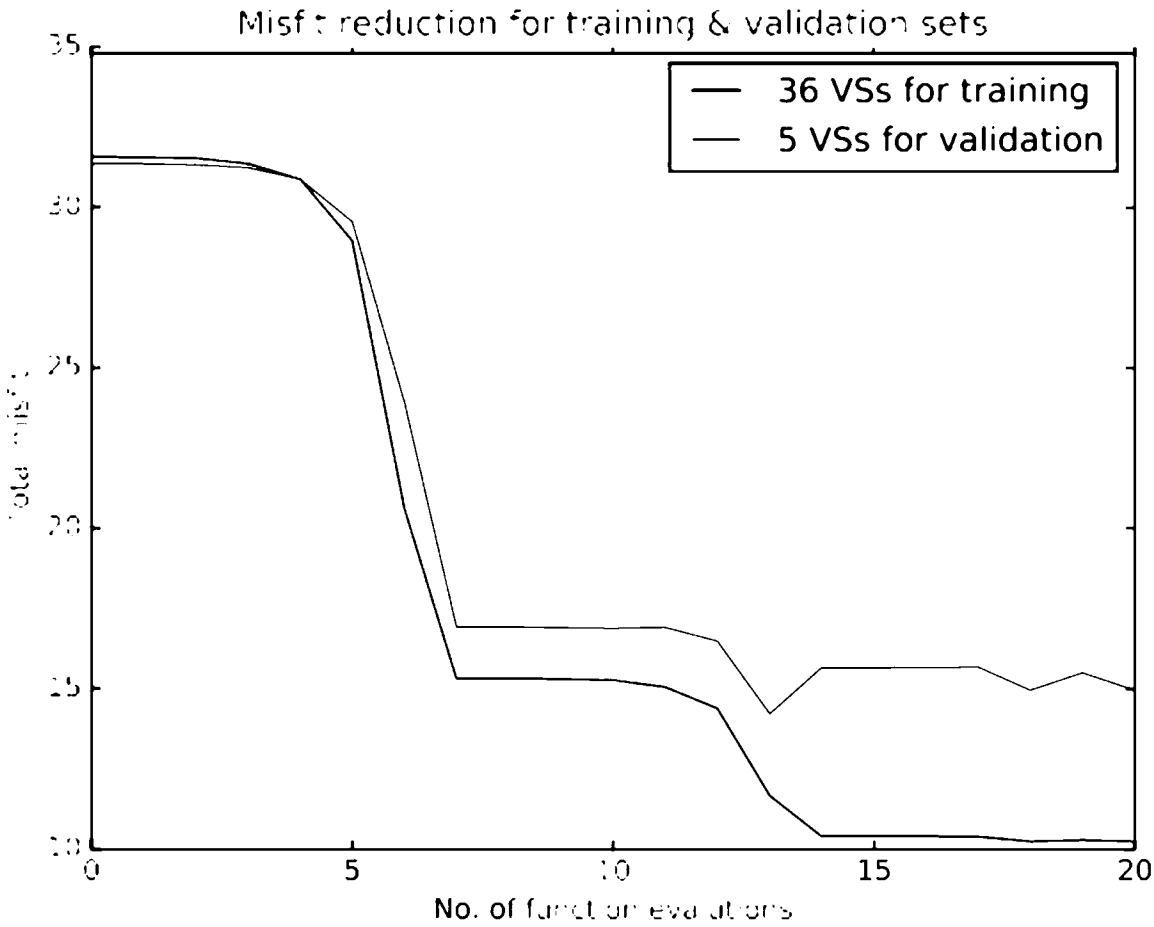
Misfit reduction for training & validation sets
36 VSs for training
5 VSs for validation
35
30
25
20
15
0
5
10
15
20
No. of function evaluations

FIG. 15

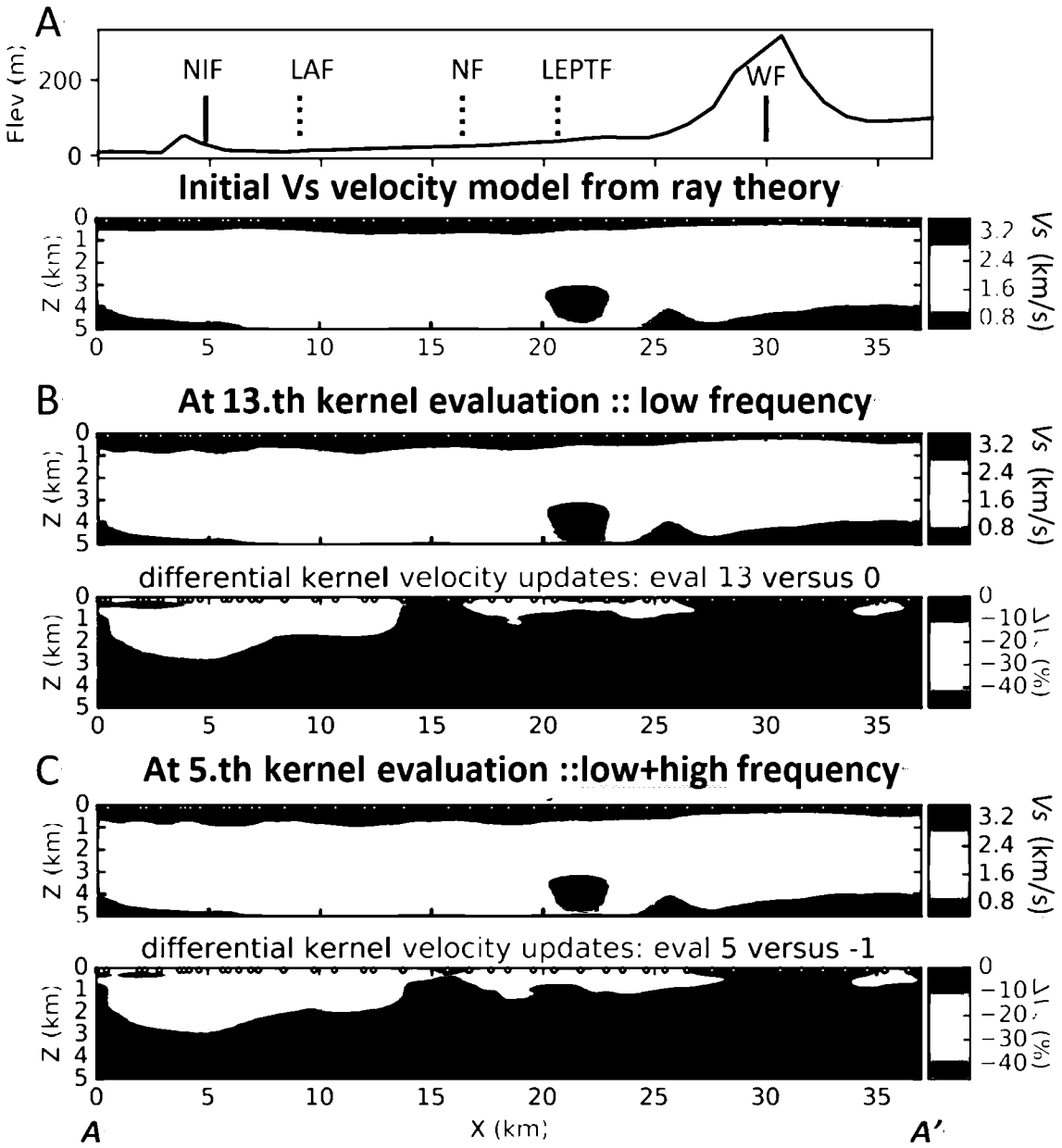
A
Elev (m)
200
0
NIF
LAF
NF
LEPTF
WF
Initial Vs velocity model from ray theory
Z (km)
Vs (km/s)
3.2
2.4
1.6
0.8
B
At 13.th kernel evaluation :: low frequency
differential kernel velocity updates: eval 13 versus 0
−10
−20
−30
−40
(%)
C
At 5.th kernel evaluation ::low+high frequency
differential kernel velocity updates: eval 5 versus -1
0 5 10 15 20 25 30 35
X (km)
A
A'

FIG. 16

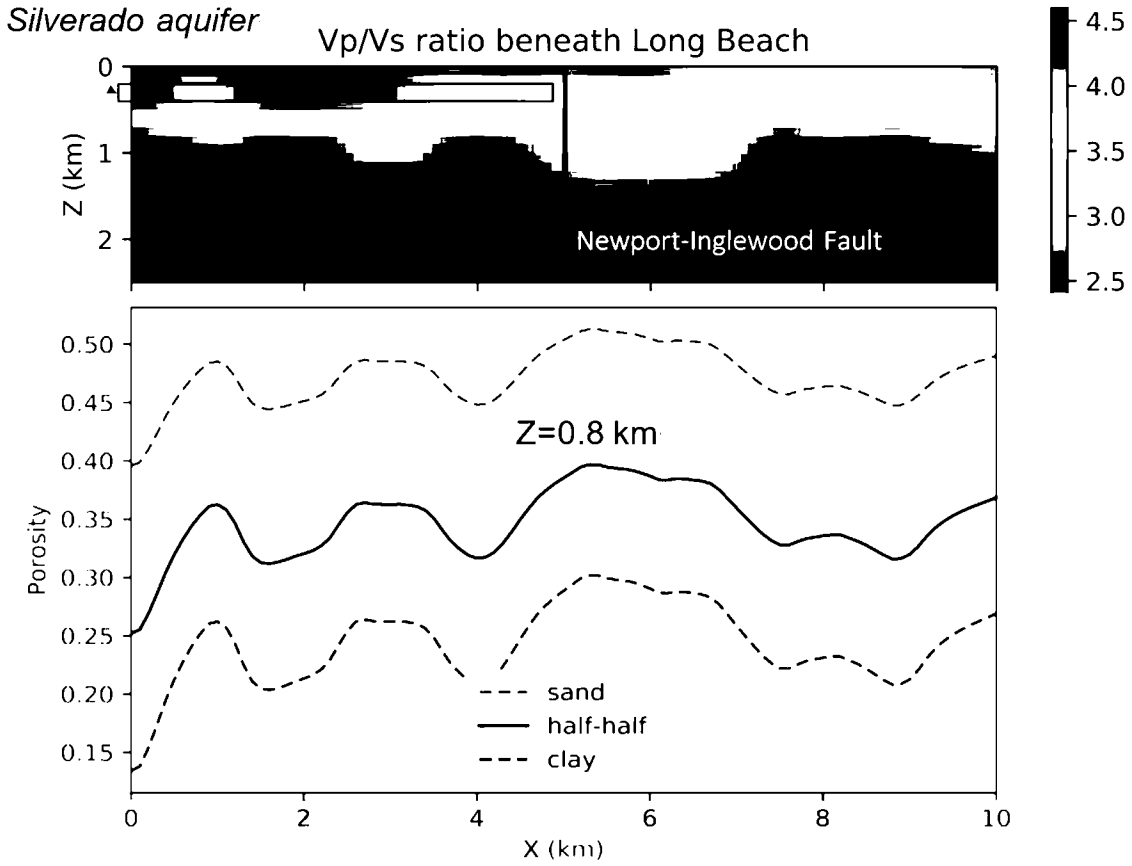
Silverado aquifer
Vp/Vs ratio beneath Long Beach
Z (km)
Newport-Inglewood Fault
4.5
4.0
3.5
3.0
2.5
Z=0.8 km
Porosity
sand
half-half
clay
X (km)

FIG. 17

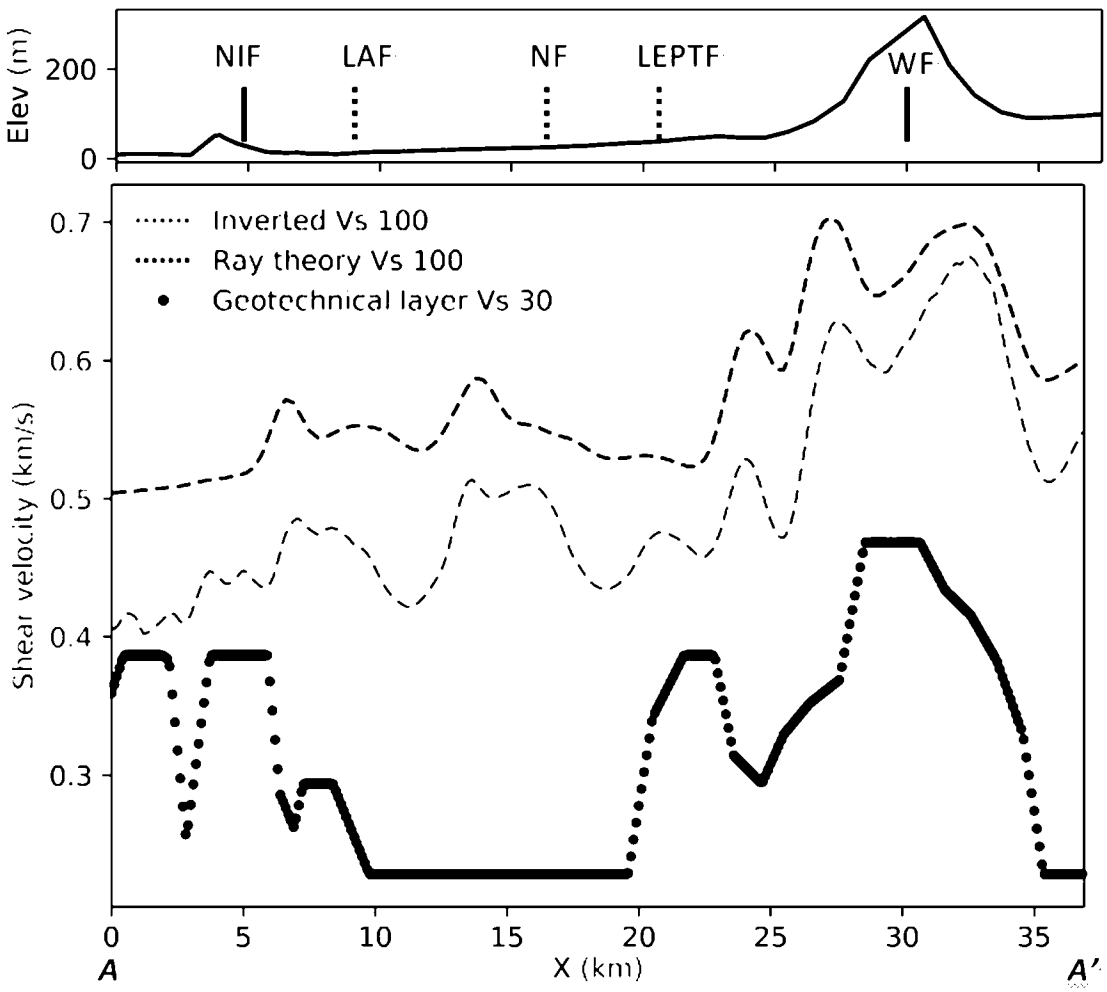
Elev (m)
200
0
NIF
LAF
NF
LEPTF
WF
Inverted Vs 100
Ray theory Vs 100
Geotechnical layer Vs 30
Shear velocity (km/s)
0.7
0.6
0.5
0.4
0.3
0
5
10
15
20
25
30
35
X (km)
A
A'

FIG. 18

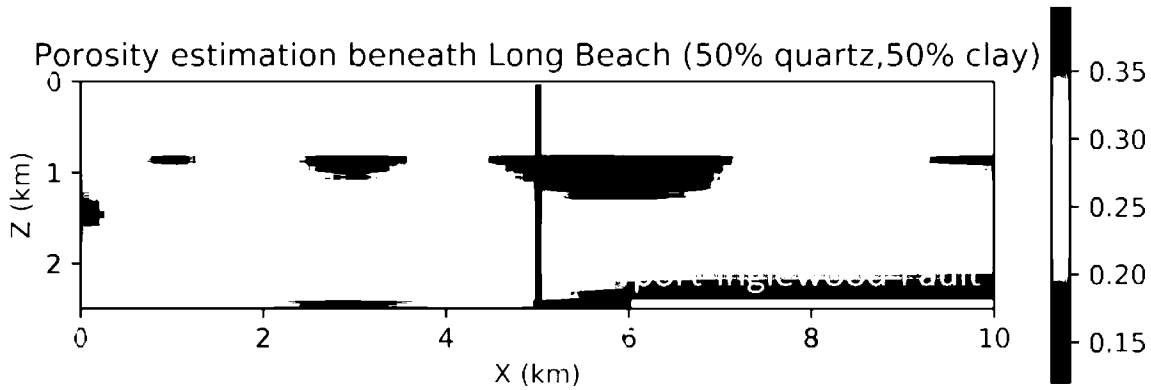
Porosity estimation beneath Long Beach (50% quartz,50% clay)
Z (km)
X (km)
0
1
2
0
2
4
6
8
10
0.35
0.30
0.25
0.20
0.15

FIG. 19

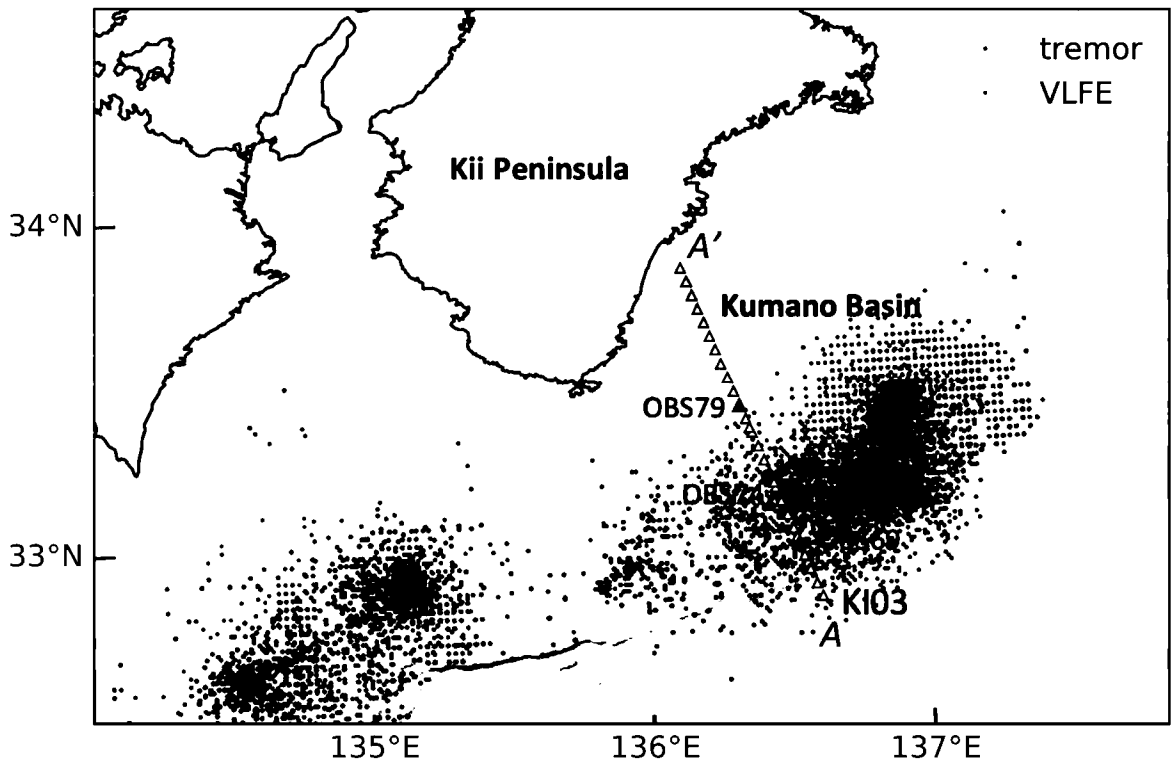
tremor
VLFE
Kii Peninsula
34°N
33°N
A'
Kumano Basin
OBS79
KI03
A
135°E
136°E
137°E

FIG. 20

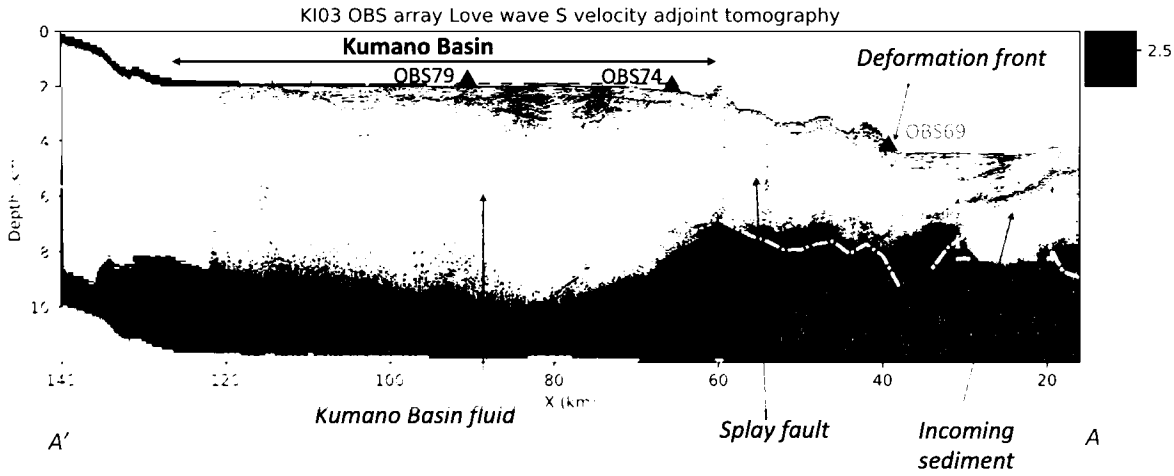
KI03 OBS array Love wave S velocity adjoint tomography
Kumano Basin
OBS79
OBS74
Deformation front
OBS69
2.5
0
Depth (km)
140
120
100
80
60
40
20
X (km)
Kumano Basin fluid
Splay fault
Incoming sediment
A'
A

FIG. 21

INTERNATIONAL SEARCH REPORT

International application No.
PCT/CN2024/101927

A. CLASSIFICATION OF SUBJECT MATTER

G01V 1/28(2006.01)i; G01V 1/30(2006.01)i

According to International Patent Classification (IPC) or to both national classification and IPC

B. FIELDS SEARCHED

Minimum documentation searched (classification system followed by classification symbols)

IPC:G01V

Documentation searched other than minimum documentation to the extent that such documents are included in the fields searched

Electronic data base consulted during the international search (name of data base and, where practicable, search terms used)

CNTXT,ENTXTC,ENTXT,VEN,CNKI: ambient noise, differential, adjoint, seismic, source, receiver, linear, dispersive, surface wave, shear wave, interferometry, synthetic

C. DOCUMENTS CONSIDERED TO BE RELEVANT

Category*	Citation of document, with indication, where appropriate, of the relevant passages	Relevant to claim No.
PX	Xin Liu et al. "Ambient noise differential adjoint tomography reveals fluid-bearing rocks near active faults in Los Angeles" *Nature Communications*, 28 October 2023 (2023-10-28), the whole document	1-14
A	US 6424920 B1 (BAKO) BAKER HUGHES INC23 July 2002 (2002-07-23) description column 3, paragraphs 1-3	1-14
A	CN 110579795 A (UYOC) UNIV CHINA OCEAN17 December 2019 (2019-12-17) the whole document	1-14
A	CN 113504566 A (CNOOC CHINA CO LTD ZHANJIANG BRANCH et al.) 15 October 2021 (2021-10-15) the whole document	1-14
A	CN 115184986 A (UYJI) UNIV JILIN14 October 2022 (2022-10-14) the whole document	1-14
A	US 2010054083 A1 (STORK CHRISTOF) 04 March 2010 (2010-03-04) the whole document	1-14

☑ Further documents are listed in the continuation of Box C. ☑ See patent family annex.

* Special categories of cited documents:
"A" document defining the general state of the art which is not considered to be of particular relevance
"D" document cited by the applicant in the international application
"E" earlier application or patent but published on or after the international filing date
"L" document which may throw doubts on priority claim(s) or which is cited to establish the publication date of another citation or other special reason (as specified)
"O" document referring to an oral disclosure, use, exhibition or other means
"P" document published prior to the international filing date but later than the priority date claimed
"T" later document published after the international filing date or priority date and not in conflict with the application but cited to understand the principle or theory underlying the invention
"X" document of particular relevance; the claimed invention cannot be considered novel or cannot be considered to involve an inventive step when the document is taken alone
"Y" document of particular relevance; the claimed invention cannot be considered to involve an inventive step when the document is combined with one or more other such documents, such combination being obvious to a person skilled in the art
"&" document member of the same patent family

Date of the actual completion of the international search	Date of mailing of the international search report
27 September 2024	**27 September 2024**

Name and mailing address of the ISA/CN	Authorized officer
CHINA NATIONAL INTELLECTUAL PROPERTY ADMINISTRATION **6, Xitucheng Rd., Jimen Bridge, Haidian District, Beijing 100088, China**	**RONG,YangMing** Telephone No. **(+86) 010-62085724**

INTERNATIONAL SEARCH REPORT

International application No.
PCT/CN2024/101927

C. DOCUMENTS CONSIDERED TO BE RELEVANT

Category*	Citation of document, with indication, where appropriate, of the relevant passages	Relevant to claim No.
A	US 2017307772 A1 (JUTILA HEIKKI ARMAS et al.) 26 October 2017 (2017-10-26) the whole document	1-14

INTERNATIONAL SEARCH REPORT
Information on patent family members

International application No.
PCT/CN2024/101927

Patent document cited in search report			Publication date (day/month/year)	Patent family member(s)			Publication date (day/month/year)
US	6424920	B1	23 July 2002	FR	2798737	A1	23 March 2001
				CA	2318627	A1	17 March 2001
				GB	0022594	D0	01 November 2000
				GB	2357144	A	13 June 2001
				GB	2357144	B	18 June 2003
				AU	5792100	A	22 March 2001
				AU	768334	B2	11 December 2003
CN	110579795	A	17 December 2019	None			
CN	113504566	A	15 October 2021	None			
CN	115184986	A	14 October 2022	None			
US	2010054083	A1	04 March 2010	US	8358562	B2	22 January 2013
US	2017307772	A1	26 October 2017	BR	112018070330	A2	12 January 2021
				BR	112018070330	B1	25 April 2023
				GB	201818642	D0	02 January 2019
				GB	2565018	A	30 January 2019
				GB	2565018	B	25 August 2021
				WO	2017184340	A1	26 October 2017
				NO	20181412	A1	05 November 2018
				SA	518400196	B1	12 May 2022
				US	10126448	B2	13 November 2018